2015

Dosimetric Advantages of Personalized Phantoms for Quality Assurance and Research in Radiation Dose Measurements

Andrew Michael Halloran
Louisiana State University and Agricultural and Mechanical College, ahallo1@lsu.edu

DOSIMETRIC ADVANTAGES OF PERSONALIZED PHANTOMS FOR QUALITY ASSURANCE AND RESEARCH IN RADIATION DOSE MEASUREMENTS

A Thesis

Submitted to the Graduate Faculty of the
Louisiana State University and
Agricultural and Mechanical College
in partial fulfillment of the
requirements for the degree of
Master of Science

in

The Department of Physics and Astronomy

by
Andrew M. Halloran
B.S., Louisiana State University, 2011
December 2015

Acknowledgements

I would like to thank my advisor, Dr. Wayne Newhauser, for his guidance throughout the course of this project and my graduate education as a whole. I would also like to thank my advisory committee members: Mr. Connel Chu, Drs. Robert Carver, James Matthews, Rui Zhang, and Vince Wilson for their advice and support.

I would like to thank the medical dosimetrists, physics staff and medical physics residents at Mary Bird Perkins Cancer Center for their assistance in conducting this project. Additionally, I would like to thank my peers for the advice, support, and discussion they provided. In particular, I thank Will Donahue, Paul Maggi, and Joe Steiner for their support over the past year.

Last, a special thanks to my wife, Priscilla, for all of the love and support she has shown me as I pursued my graduate degree.

Table of Contents

List of Tables

List of Figures

Abstract

Background: Phantoms have been in use in medical and health physics for decades, serving as a surrogate for human tissue in several different applications. In radiation dose measurements, anthropomorphic phantoms are designed with tissue substitute materials to mimic both the elemental compositions and anatomical structures of the human body. In some cases the performance of anthropomorphic phantoms for personalized measurements is severely limited by the use of reference anatomy in the geometric design. 3D printing could potentially be used to overcome some of these shortcomings by enabling rapid fabrication of personalized phantoms for individual patients based on radiographic imaging data. The aim of this work is to determine whether 3D-printed phantoms are a feasible means of performing patient-specific dosimetric measurements for electron beam radiotherapy.

Methods: We measured dose distributions from 6 to 20 MeV electron beams impinging on a variety of materials and geometries to determine the radiological properties of 3D printed phantoms. The water equivalent thickness of homogeneous molded and printed slabs were determined from depth dose measurements. Molded and Printed anthropomorphic slabs were compared for equivalency in electron beam penetration range properties using gamma index analysis with the criteria of 3% dose difference or 3 mm distance to agreement. Last, a personalized head phantom was printed and compared with a reference phantom using gamma index analysis for use in electron beam dose calculations using a treatment planning system.

Results: The printed personalized phantom provided superior dosimetric accuracy compared to the molded reference phantom. Personalized 3D printed radiotherapy phantoms achieved a pass rate of greater than 60% for electron beam radiotherapy treatments using 16 and 20 MeV electron energies.

Conclusion: Creating personalized phantoms using 3D printing techniques is a feasible way to substantially improve the accuracy of dose measurements of therapeutic electron beams. Further improvements are necessary in order to increase the dynamic range of mass densities that are achievable with printing, e.g., low density lung and high density bone.

Chapter 1:Introduction

1.1. Phantoms in Medical and Health Physics

One of the most common methods of treating cancer is the use of external beam radiotherapy, with approximately half of all cancer patients receiving radiotherapy at some point during their course of treatment (Smart 2000). The quality of radiation therapy treatments are checked with dose measurements in phantoms, which are defined as inanimate surrogates for a human body or anatomic region of interest with the purpose to mimic human tissue for a specific procedure or experiment (DeWerd and Kissick 2014). Phantoms can be divided into two categories: computational phantoms and physical phantoms.

1.1.1. Computational Phantoms for Dose Calculations

Computational phantoms are utilized for internal and external dose assessments (Lee et al. 2007, Menzel, Clement, and DeLuca 2008, Newhauser et al. 2009). Computational anthropomorphic phantoms can represent the human body with arbitrary detail of the anatomical geometry and composition of human tissue. These phantoms are often utilized for radiotherapy dose calculations, such as the example shown in Figure 1.1. The benefit of computational anthropomorphic phantoms in radiation therapy dose calculations is that they can be geometrically customized to match individual patient anatomy, providing an improved means of performing dose calculations to individual organs or regions of interest.

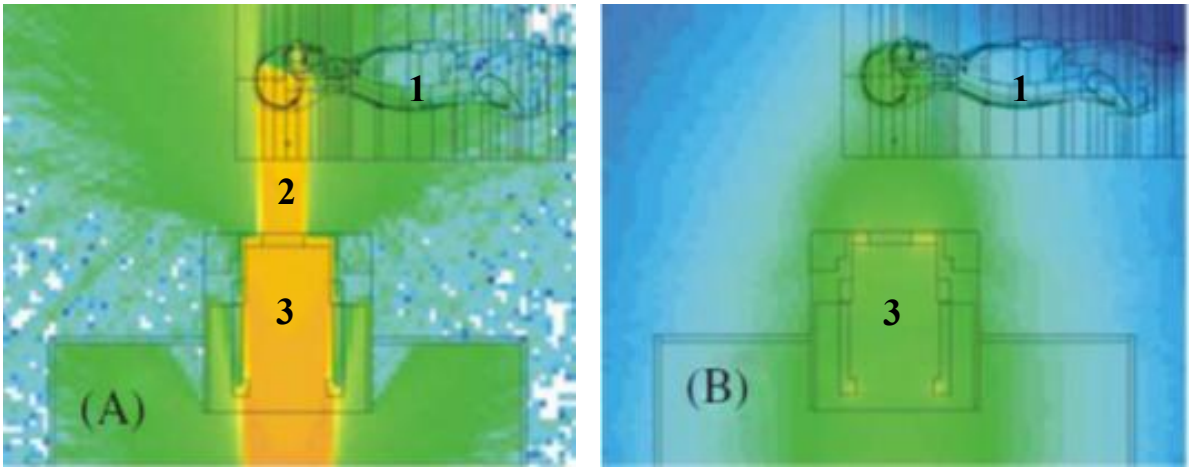

Figure 1.1. An illustration of a computational anthropomorphic phantom. This phantom was used in simulating doses from proton therapy treatments for craniospinal cancers. The color mapping shows fluence intensity, with orange being the highest and dark blue being the lowest. Figure (A) shows the shows the primary and secondary proton fluence, and Figure (B) shows the neutron fluence. The images include (1) the computational phantom, (2) the proton beam, and (3) the treatment machine. Image adapted from Newhauser et al. (2009).

1.1.2. Physical Phantoms for Dose Measurements

Phantoms are used in radiation oncology to perform a variety of radiation dose measurements. Phantoms vary in terms of their composition, shape, and function depending on the role they are designed to fill. Scanning water tanks and water equivalent plastic slabs are heavily utilized in the quality assurance of medical linear accelerators, as detailed in the report of AAPM Task Group 51 (Almond et al. 1999). Various types of dosimeters (film, diodes, ionization chambers) and tissue substitute phantoms are used for radiation therapy quality assurance in order to verify that the prescribed therapeutic doses are properly delivered (McKenzie et al. 2014). Organ motion phantoms, such as the motorized phantom used to simulate lung motion in a study by in Eley et al. (2014), can replicate periodic organ motion to investigate methods to treat moving tumors (Bert and Durante 2011).

1.1.3. Physical Anthropomorphic Phantoms

Anthropomorphic phantoms mimic the internal and external anatomy of the human body (Figure 1.2). While the goal of the anthropomorphic phantoms is to achieve equivalency in radiation interaction properties with human tissues, in general they fail to achieve complete equivalence. Most phantoms are designed using reference anatomy, such as that which is described in ICRP Reports 23 and 89 (1975, 2002).

Physical anthropomorphic phantoms provide a medium in which to measure radiation distributions in human-like anatomy. Common uses of these phantoms include the validation of new therapeutic techniques and investigations where anatomical features are potentially important.

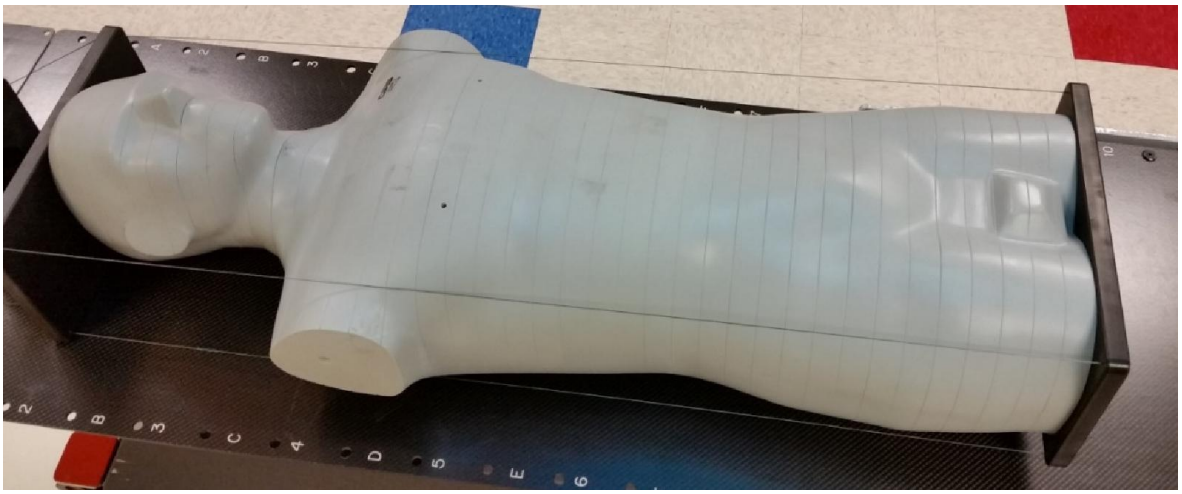

Figure 1.2. An anthropomorphic adult male phantom designed from reference anatomy. This phantom was constructed from multiple tissue equivalent epoxy resins and fabricated using molds. The design is compatible multiple types of dosimeters.

1.2. 3D Printing

1.2.1. Overview of 3D Printing

3D printing, also known as rapid prototyping, is the use of additive fabrication methods to construct three-dimensional structures (Wong and Hernandez 2012). The structure design is rendered as tessellated 3D surface mesh, and can be generated using several different types of 3D computer-automated design programs. These computer-rendered surface meshes are formed with triangles identified by three vertices and a normal vector to form water-tight solids, which are uploaded to 3D printing units as surface tessellation language (STL) files (Rengier et al. 2010). The orientation of the normal vector specifies the outer surfaces and creates the boundary of the structure. STL input files are then parsed into layers for printing.

There are several different approaches of additive manufacturing outlined in detail in a review of the technology by Wong and Hernandez (2012). Printed structures may take a wide variety of geometries with up to micrometer resolution. 3D printers use a wide range of materials, including polymers, thermoplastics, and several types of metals. A summary of the fabrication methods capable of printing nonmetal filaments is listed in Table 1.1. This study exclusively focused on the fused deposition method. This printing process is the layer-by-layer deposition of a molten filament to build structures. The filament is heated beyond its glass transition temperature and then extruded. Some of the available filaments for fused deposition printing include nylon, acrylonitrile butadiene styrene (ABS), and polycarbonate.

Table 1.1. A summary of different additive fabrication methods.

3D Printing Modality	Description
3DP	Fabrication of 3D structures through the layer-by-layer adhesion of powdered polymers.
Stereolithography	Solidification of structures via photopolymerization of liquid polymers using ultraviolet laser radiation.
Fused Deposition Modeling	Fabrication of 3D structures through the layering of heated thermoplastic filament.
Selective Laser Sintering	Use of a CO_2 laser to sinter loose filament particles together to form structures. Large variety of printable filaments.
Electron Beam Melting	Use of a free electron laser to sinter loose filament particles together to form structures. Large variety of printable filaments.
Laminated Object Manufacturing	Laminates sheets of material together in layers, then refines structure shape through CO_2 laser subtraction.
Polyjet	Use of inkjet technology to deposit photopolymers, which are cured by ultraviolet lamps.

1.2.2. 3D printing Applications in Radiation Oncology

3D printing has been utilized in a growing number of applications in radiation oncology, including printing molds for creating intensity-modulated radiation therapy compensator blocks or proton therapy range compensator blocks (Avelino, Silva, and Miosso 2012, Ju et al. 2014). Other applications have focused on the use of imaging data for the design of printed structures, such as the development of immobilization devices for x-ray treatments for head and neck cancers. Fisher et al. (2014) tested the feasibility of printing these immobilization devices as an alternative to the current clinical standard of thermoplastic masks fitted to the patient. The benefit of using 3D printing to produce these devices is that they would avoid the discomfort caused as a traditional thermoplastic mask is stretched over the patient.

1.2.3. 3D Printed Phantoms for Radiation Dose Measurements

3D printing of phantoms for radiation dose measurements is of increasing interest as printing technology improves and fabrication costs fall. In some studies, 3D printing has been used to create positive molds for custom geometry dosimeters. A recent work by Bache et al. (2015) used 3D printed molds designed from rat imaging data to create rodent-morphic leuco-dye doped plastic 3D (Presage, Skillman, NJ) dosimeters with high density inserts to model internal heterogeneities. Another method of using 3D printing technology for dose measurements has been to print anatomical regions with plastics that have similar properties to human tissue. Ehler et al. (2014) proved that 3D printing could feasibly be used as a fabrication technique to develop patient-specific phantoms for quality assurance in photon radiotherapy (Figure 1.3). A benefit of this method of creating radiotherapy phantoms is that the structure designs can be modified to fit multiple types of dosimeters, such as added film planes or cavities for ionization chambers.

Figure 1.3. A 3D printed head phantom designed from imaging data. This phantom was adapted in post-processing to be able to utilize multiple forms of dosimeters, and printed with ABS plastic using fused deposition modeling. Image adapted from Ehler et al., (2010).

1.3. Electron Radiotherapy

Electron beam radiotherapy is used in the treatment of superficial or shallow diseases. This charged particle therapy has been most commonly delivered using microwave-based electron linear accelerators for the past four decades (Hogstrom and Almond 2006). Electron linear accelerators are used to deliver both electron and photon therapy treatments, and are the most common type of treatment.

The benefit of electron beam therapy comes in the depth dose distribution properties of electron beams, which is plotted in Figure 1.4. Therapeutic electron beams show a quick rise to the maximum dose at depth, d_{max}, then exhibit a sharp falloff. The shape of the dose distribution varies with electron beam energy, field size, and target medium. Electron therapy is ideal for treating many superficial diseases because it spares distal healthy tissues from unnecessary radiation exposure. Some indications of electron therapy include lesions of the head and neck, skin, and chest wall cancers, as well as boost treatments (Hogstrom and Almond 2006). Modern electron radiotherapy treatment planning uses the pencil-beam algorithm (PBA) developed by Hogstrom, Mills, and Almond (1981), which utilizes the Fermi-Eyges multiple coulomb scattering theory for modeling dose in patients while accounting for field size, density variations, air gaps, and irregular surface anatomy.

Internal tissue heterogeneities and irregular external surfaces can have a profound effect on the dose distributions at depth in the patient (Hogstrom and Almond 2006, ICRU 1984a). Irregular surfaces can affect the flatness of the dose distribution while tissue heterogeneities such as bone-tissue or soft tissue-lung interfaces can affect both the charged particle equilibrium and range of electron beams. These can negatively impact coverage of the planning target volume (PTV) and the absorbed dose to healthy tissues both lateral and distal to the PTV.

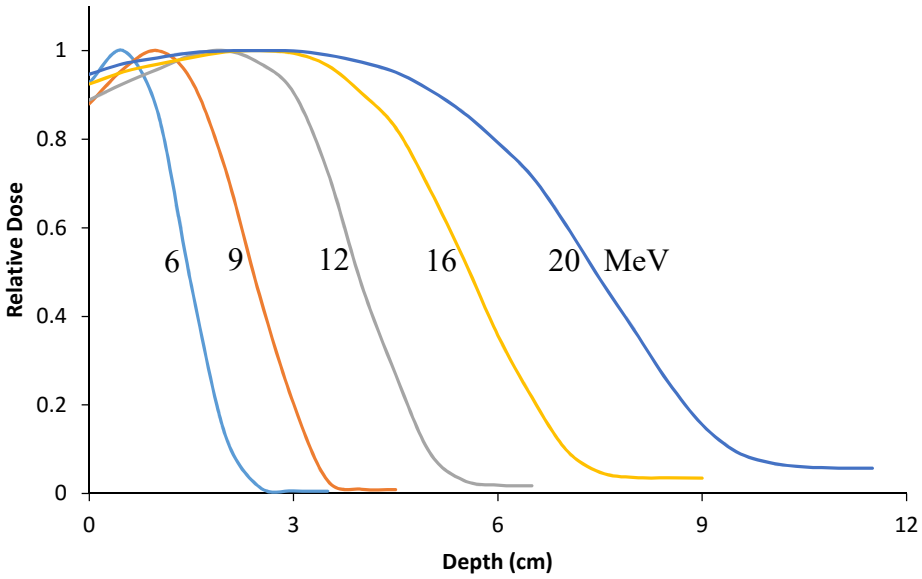

Figure 1.4. Measured depth dose distributions for 6, 9, 12, 16, and 20 MeV therapeutic electron beams. The distributions show initial increase in relative dose, followed by distal falloff and the bremsstrahlung x-ray tail. The sharpness of the distal falloff slope decreases with increasing beam range.

1.4. Statement of the Problem

While significant improvements in computational anthropomorphic phantom designs have been made over the past several years, there is still room for improvement in the fabrication of anatomical features in physical phantoms. In some cases reference phantoms inadequately mimic anatomical features of individual patients. Many of these features are either averaged out or omitted in the fabrication process due to the use of reference anatomy as a design basis or the difficulty of fabricating such features using traditional manufacturing methods. Examples of patient-specific anatomical features include sinus cavities, congenital defects, surgical amputations, implanted devices, large tumors, growth abnormalities, and bony processes such as the petrous ridge of the temporal bone of the cranium.

1.5. Hypothesis and Specific Aims

In order to determine whether personalized 3D printed radiotherapy phantoms could provide the capabilities of reference anthropomorphic phantoms, but with improved dosimetric accuracy, we tested the following hypothesis: A personalized 3D printed phantom can achieve a pass rate of greater than 60% for electron beam radiotherapy treatments with a gamma index analyses criteria of 3% dose difference or 3 mm distance to agreement.

In order to test this hypothesis, we performed the following specific aims:

Aim 1: Compare 1D relative absorbed dose distributions and physical properties of homogeneous slabs of molded reference materials and homogeneous slabs of printed material.

Aim 2: Compare 2D relative absorbed dose distributions in printed and molded anthropomorphic phantom slabs.

Aim 3: Compare 3D relative absorbed dose distributions in personalized and reference head phantoms.

Chapter 2: Methods

2.1. Aim 1: Comparison of Phantom Materials and Fabrication Techniques

In the first aim, homogenous molded slabs of selected reference tissue substitute materials were compared to homogenous 3D printed slabs of tissue substitute plastic. The printed slabs were designed to have the water equivalent thickness (WET) as the molded slabs. This was accomplished by first designing and printing a series of printed slabs with the same WET as the reference slabs, then measuring the WET using therapeutic electron beams. The physical properties of the printed slabs were quantified using dimension and mass measurements. The goal of this aim was to verify that 3D printed objects can achieve the same range shifting properties as the molded reference objects.

2.1.1. Reference Molded Slabs and 3D Printed Slabs

For this work, an adult male generic anthropomorphic phantom (Model 701-C ATOM® Adult Male Dosimetry Phantom, S/N 701-L1692, CIRS, Inc., Norfolk, VA) molded from epoxy resins was selected as the reference phantom. The maximum and minimum densities of this phantom, as stated by the manufacturer, are 0.21 g/cm^3 and 1.60 g/cm^3 for lung and bone, respectively. In order to replicate the radiological properties of generic phantoms, we selected reference materials near to the minimum and maximum tissue densities in the reference phantom. A section of homogeneous lung tissue from an adult reference phantom was selected for the low density material. This material is molded out of an epoxy resin with a mass density of 0.21 g/cm^3 and a thickness of 2.5 cm. To represent the bone we selected a 2.54 cm thick slab of polyoxymethylene (DELRiN Rectangular Bar NAT, Lot 4252285, Quadrant Engineering Plastic Products, Reading, PA), with a density of 1.41 g/cm^3. This thermoplastic has a density that is close to that of the bone substitute (epoxy resin) used in the reference phantom (1.60 g/cm^3). The

3D printer filament used in this work is Polylactic acid, or polylactide (PLA). PLA (Prototype Supply 3 mm PLA filament, Lot 20140601AD, ToyBuilder Labs, Pasadena, CA) is a thermoplastic derived from sugars found in organic matter such as corn starch, sugarcane, or other plants with a high sugar content. The density and chemical composition of amorphous PLA are 1.24 g/cm^3 and $(C_6H_8O_4)_n$, respectively.

For each reference slab, the water equivalent thickness (WET) was calculated following the methods described in Zhang and Newhauser (2009), or

$$t_w = t_m \cdot \frac{\rho_m}{\rho_w} \cdot \frac{\overline{\left(S/\rho\right)}_m}{\overline{\left(S/\rho\right)}_w} \ (cm), \tag{2.1}$$

where t_m is the thickness of the reference slab, ρ_m is the density of the reference slab, ρ_w is the density of water, $\overline{\left(S/\rho\right)}_m$ is the average mass stopping power in the reference slab, and $\overline{\left(S/\rho\right)}_w$ is the average mass stopping power in water. This WET method was used to compare the range shifting characteristics of electrons traversing various slabs for nominal electron energies of 6, 9, 12, 16, and 20 MeV.

The mass stopping powers for water, the reference bone slab, and the reference lung slab were determined from Berger et al. (2005), who calculated the mass stopping powers using ICRU 37 methodology (ICRU 1984b). The mass stopping power values are tabulated in Table 2.1. To verify the accuracy of the WET calculations, the values were also calculated following the methods described in IAEA Technical Report 398 (2000),

$$z_w = z_{pl} * c_{pl} = z_{pl} * \frac{R_{CSDA,w}}{R_{CSDA,pl}} \left(g/cm^2\right), \quad 2.2$$

Where z_w is the WET, z_{pl} is the material thickness, and c_{pl} is the ratio of electron continuous slowing down approximation (CSDA) ranges for water and the reference material, $R_{CSDA,w}$ and $R_{CSDA,pl}$. $R_{CSDA,w}$ and $R_{CSDA,pl}$ were taken from Berger et al. (2005). It should be noted that although Equations 2.1 and 2.2 exclude electron scattering from the WET calculations, this is an acceptable assumption for the energy range studied because the electron energy loss in water is approximately 2 MeV per cm with little variation between electron beam energies.

Table 2.1. The total mass stopping powers, stopping power ratios, and water equivalent thicknesses for the reference slabs. The electronic stopping powers are the sum of both the radiative and collisional stopping powers, with an uncertainty of up to 2% for collisional stopping powers and 5% for radiative stopping powers for electrons ranging between 2 and 50 MeV (ICRU 1984b).

Energy (MeV)	$\overline{(S/\rho)}$ (MeV*cm^2/g)				$\overline{(S/\rho)}_m/\overline{(S/\rho)}_w$		Calculated t_w (mm)	
-	Water	Ref. Lung	Ref. Bone	PLA	Ref. Lung	Ref. Bone	Ref. Lung	Ref. Bone
6	2.010	2.045	1.907	1.895	1.017	0.949	5.341	33.979
9	2.116	2.150	2.008	1.996	1.016	0.949	5.334	33.986
12	2.214	2.245	2.100	2.088	1.014	0.949	5.324	33.970
16	2.337	2.361	2.216	2.201	1.010	0.948	5.304	33.960
20	2.454	2.472	2.326	2.310	1.007	0.948	5.289	33.946

The physical thicknesses of the printed slabs were determined using

$$t_{m,PLA} = t_w \cdot \frac{\rho_w}{\rho_{PLA}} \cdot \frac{\overline{(S/\rho)}_w}{\overline{(S/\rho)}_{PLA}} \ (cm), \quad 2.3$$

where $t_{m,PLA}$ is the PLA thickness, ρ_{PLA} is the density of PLA filament, and $\overline{(S/\rho)}_{PLA}$ is the average mass stopping power of electrons in homogeneous PLA. t_w is the calculated WET value

listed in Table 2.1. This equation was derived from Equation 2.1. The calculated $t_{m,PLA}$ values are listed in Table 2.2.

Table 2.2. The calculated thicknesses, $t_{m,PLA}$, for the printed slab phantoms. The values were calculated using the average mass stopping powers and water equivalent thicknesses listed in Table 2.1.

Energy (MeV)	Calculated $t_{m,PLA}$ (mm)	
-	Ref. Lung	Ref. Bone
6	4.569	29.065
9	4.561	29.056
12	4.552	29.048
16	4.542	29.079
20	4.531	29.082

Using the calculated $t_{m,PLA}$ values, three different printed slabs were designed using commercially available CAD software (AutoCAD Professional 2015, Autodesk, Inc., Mill Valley, CA). Slabs designed for each $t_{m,PLA}$ were not necessary because the variations in thickness across the range of electron energies are smaller than the printer tolerance of ± 2 mm. Each slab had a length and width of 80 mm to allow for conditions of lateral equilibrium in the range shift measurements. Two slabs were designed to have the same calculated WET as the lung reference slab (L_{ref}). The first was a 4.55 mm thick solid printed slab ($L_{p,\,100\%}$), whose thickness was determined from the average of the t_{PLA} values listed in Table 2.2 for all electron beam energies. The second slab was a 25 mm thick printed slab ($L_{p,\,16.8\%}$) with a reduced infill density, where the percentage subscript represents the slab infill density. $L_{p,\,16.8\%}$ was designed with the intent of matching the lung reference material in WET, physical thickness, and average mass density. The infill density for this slab was 16.8%, which was determined using the ratio of

the densities of the reference lung slab and PLA filament. The final printed slab was designed to replicate the radiological thickness of the bone reference material; this printed slab ($B_{p,\ 100\%}$) had a thickness of 29.07 mm. The slabs were printed in-house using a manufacturer-recommended extruder and bed temperature of 210°C and 70 °C, respectively, and a layer height of 0.4 mm. All three slabs were printed with PLA using the grid infill pattern. The reference and printed slab properties are listed in Table 2.3.

Table 2.3. The description and physical properties for the reference and printed slabs. The listed physical properties for the reference materials are the manufacturer stated values. The listed physical properties for the printed slabs are design parameters.

Slab	Reference Material	Fabrication Material	Fabrication Process	t_m (mm)	Density (g/cm^3)	Infill Density (%)	ρt_m (g/cm^2)
L_{ref}	-	Epoxy resin	Molded	25	0.21	100	0.525
$L_{p,\ 100\%}$	Lung	PLA	Printed	4.55	1.24	100	0.564
$L_{p,\ 16.8\%}$	Lung	PLA	Printed	25.0	0.21	16.8	0.525
B_{ref}	-	POM	Molded	25.4	1.41	100	3.581
$B_{p,\ 100\%}$	Bone	PLA	Printed	29.07	1.24	100	3.605

To investigate how printer settings influence the mass density, a series of similar slab phantoms were printed with different settings for “infill” density and layer height. Infill density is a correction factor applied to the printed structure density which affects the lateral filament spacing in a printed structure, while varying the layer height affects the total number of layers and the size of the microscopic air pockets formed during the layering process (Figure 2.1). In the printer interface software, the print settings for infill density and layer height were varied between minimum and maximum values to quantify their effects on printed infill pattern and average mass density (Table 2.4).

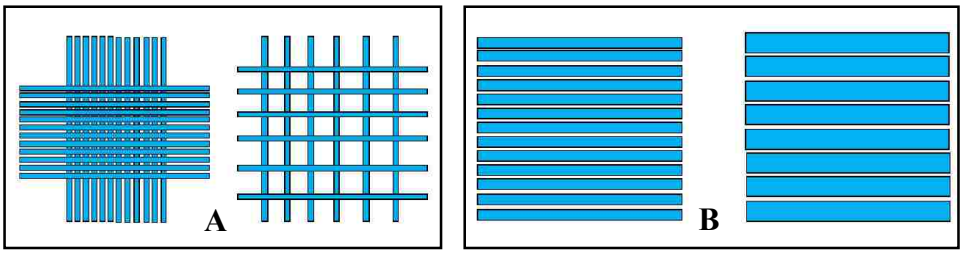

Figure 2.1. Graphics depicting the impact of varying the infill density and layer height for a printed structure. Varying the infill density (A) affects the spread of filament lines in the structure, introducing air cavities to reduce the average mass density. Varying the layer height (B) impacts alters the height of each stacked layer, which can increase or reduce the microscopic mass density variations that occur in the layering process.

Table 2.4. The design specifications for each of a series of four slab phantoms. Slabs T1 and T2 were designed to examine the effect that layer height has on mass density. Slabs T3 and T4 were designed to determine the minimum and maximum mass densities the 3D printer can achieve.

Slab	**Layer Height**	**Infill Density**
-	(mm)	(%)
T1	0.20	50
T2	0.40	50
T3	0.20	100
T4	0.40	10

The slabs in this study were printed in-house using a fused-deposition 3D printer (AW3D XL, AirWolf 3D, Costa Mesa, CA). To print the slabs, the slab STL file was imported into the printer interface software (MatterControl version. 1.2, MatterHackers Inc., Lake Forest, CA). Each slab was printed with PLA filament using the previously specified extruder and bed temperatures. A grid infill pattern was selected for this study because, of the available infill pattern options, it provided the most suitable internal structure for achieving laterally uniform mass density (Figure 2.2).

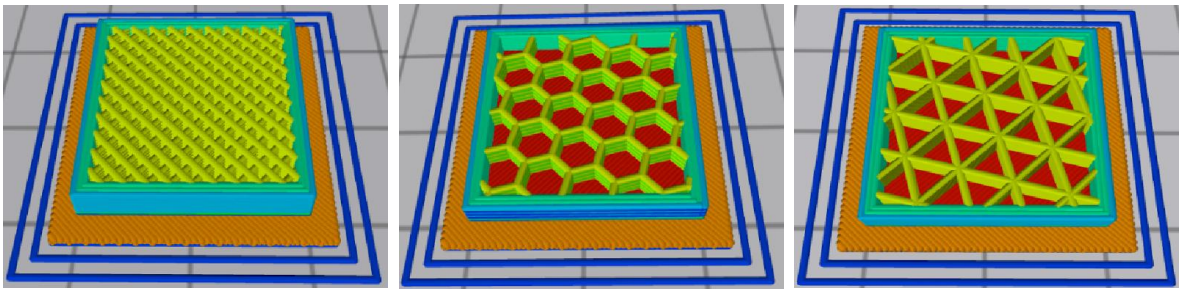

Figure 2.2. Examples of the different fill patterns available in the printer interface software. From left to right, the fill patterns shown are grid infill, hexagonal infill, and triangular infill. Images adapted from matterhackers.com.

Each printed slab was weighed and measured for length, width, and thickness in order to calculate its average mass density. The dimensions were measured using a digital caliper with an uncertainty of 0.01 mm (Pro-Max NSK Electronic Digital Caliper, Fowler High Precision, Newton, MA). The mass of each slab was measured using a digital scale with an uncertainty of 50 mg (Scout II Digital Scale, S/N SC4010, Ohaus Corporation, Parsippany, NJ). For each slab, the average mass density was determined from $\rho = {}^{m}/_{V}$. The calculated density was reduced by subtracting the estimated mass and volume of each (solid) sidewall, which was accomplished through dimensional measurements of the filament layer width for each sidewall. This provided a more accurate value for the average mass density of the internal infill structure, which was in the beam path for the range shift measurements.

2.1.2. Range Measurements

We measured electron beam depth ionization curves using the reference and printed slabs in order to determine their range shifting properties. All measurements were performed using a clinical electron linear accelerator (Varian Model 21EX 6/18, S/N 1251, Palo Alto, CA) located at Mary Bird Perkins Cancer Center (MBPCC) in Baton Rouge, LA. Ionization curves were recorded using a parallel plate ion chamber (PTW TN34001 Roos Chamber, S/N 01837,

Freiburg, Germany) coupled with a digital electrometer (CNMC Model 206 Dosimetry Electrometer, S/N 11401357, Nashville, TN) in a vertical one-dimensional scanning water tank (Standard Imaging 1D Scanning Water System, REF 70800/70800E, Middleton, WI). The accelerator setup for performing the range measurements utilized a 10x10 cm^2 electron cone with a 6x6 cm^2 lead alloy (Cerrobend, MT-A158, MED-TEC, Orange City, IA) insert, with the gantry and collimator aligned to provide a perpendicular beam downward towards the treatment couch. The accelerator was calibrated following the guidelines specified in AAPM Task Group Report 51 (Almond et al. 1999). Before performing measurements, the accelerator was warmed up following the clinical protocols for daily quality assurance.

To record the depth ionization curves in water, the water tank was positioned on the treatment couch and aligned with the central axis of the beam, then allowed to equilibrate to room temperature. The ionization chamber was positioned along the central axis of the beam and leveled flush with the surface of the water. Measurements were taken vertically at 2 mm increments from the surface of the water past the end of the practical range for each electron energy. For each measurement point, 50 monitor units (MU) were delivered. This procedure was repeated for electron beam energies of 6, 9, 12, 16, and 20 MeV.

In order to measure the ionization curves through the slabs, the slabs were suspended above the water using packing tape and aligned along the central axis of the beam (Figure 2.3). The tape did not perturb the electron field. The distance from the source to the surface of the slab was then readjusted to 100 cm, and measurements were repeated using the same procedure as described for the unimpeded depth ionization curves. Depth ionization curves for the lung slabs were recorded for 6, 9, 12, 16, and 20 MeV electron beams. Depth ionization curves for the bone

slab were recorded for 12, 16, and 20 MeV electron beams; 6 and 9 MeV electron beams were omitted because they lacked sufficient range to penetrate the bone slabs.

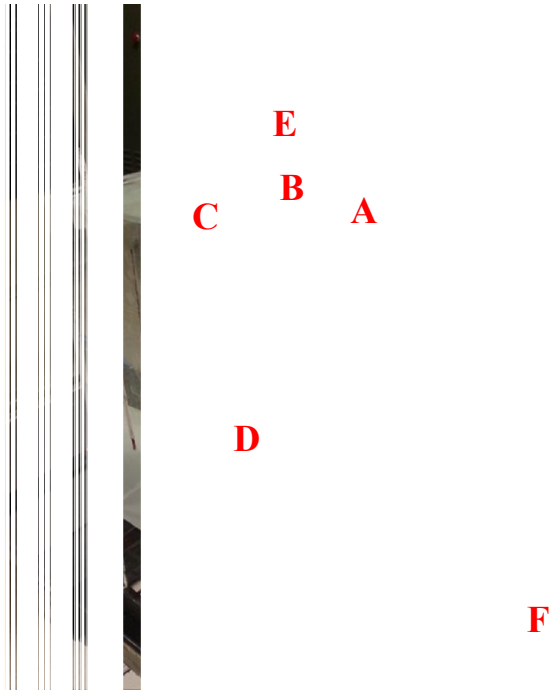

Figure 2.3. The setup used for recording depth ionization curves in water. The slab is placed on the tape support grid and aligned with the beam central axis, flush with the surface of the water. For each slab phantom and reference material, the SSD was adjusted to 100 cm. The setup includes the (A) ionization chamber holster, (B) printed slab, (C) tape grid, (D) water tank, (E) electron cone, and (F) treatment couch.

2.1.3. Modeling of Depth Ionization Curves

After being recorded, the ionization curves were entered into data analysis software (Excel 2013, Microsoft Corporation, Redmond, WA). The measured data points were corrected for temperature, pressure, and chamber wall thickness using correction methods described in AAPM Task Group 51 (Almond et al. 1999). The ionization curves for each slab were corrected for inverse square effects to account for the change in depth of the initial point of measurement. This was accomplished using the physical thickness of each slab in accordance with the methods stated described in AAPM Task Group 25 (Khan et al. 1991). The shifted ionization curves were then fitted to

$$\mathrm{I} = \mathrm{I}_{\mathrm{proximal}} \cdot \mathrm{c}_{\mathrm{distal}} + \mathrm{I}_{\mathrm{x-ray}}, \quad 2.4$$

where $I_{proximal}$ is the proximal ionization, c_{distal} is the distal scaling factor, I_{x-ray} is the bremsstrahlung ionization term. These terms and the depth ionization curve are plotted in Figure 2.4. The proximal ionization term is given by

$$I_{proximal} = m \cdot x + b + m \cdot t_w, \quad 2.5$$

where m is the slope , x is the depth in water, b is the ionization at zero depth, and t_w is the water equivalent thickness of any slab present. The distal falloff term is represented by the complimentary error function

$$c_{distal} = 1 - \frac{1}{\sigma\sqrt{2\pi}} \cdot e^{-\frac{1}{2}\left(\frac{x-(r_{50}-t_w)}{\sigma}\right)^2}, \quad 2.6$$

where r_{50} is the mean electron beam range, x is the water depth, and σ is the standard deviation, which determines the rate at which the dose falls off with depth near the end of range. The bremsstrahlung ionization term is given by

$$I_{x-ray} = \alpha \cdot e^{-\mu(x+t_w)}, \quad 2.7$$

where α is the magnitude and μ is the attenuation coefficient of the bremsstrahlung radiation in water. Any additional bremsstrahlung radiation generated in the water is considered to be negligible and excluded from Equation 2.7.

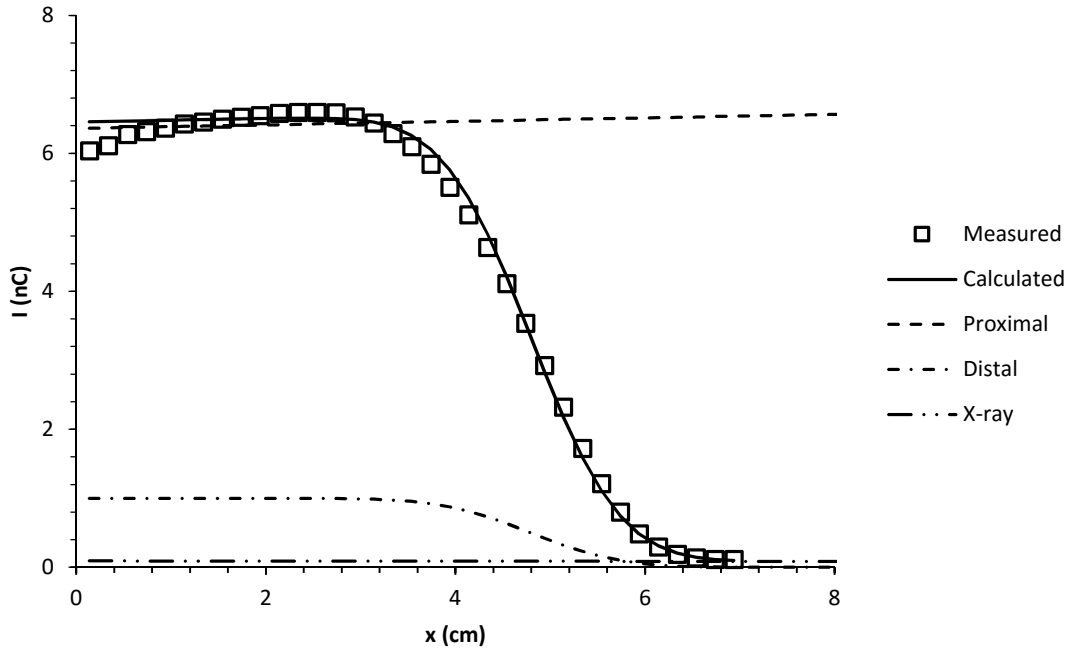

Figure 2.4. A graph of the measured and fitted ionization I versus water depth x for a 12 MeV electron beam. The calculated ionization is most heavily influence by the proximal and distal components.

The model parameters σ, r_{50}, m, b, α, μ, and t_w were determined by fitting the measured data to Equation 2.4. To fit the measured ionization curves in water with no material present, t_w was set to 0 and all of the other modeling parameters were allowed to vary. For ionization curves recorded with a slab present, only t_w and b were allowed vary from the values for the fitting parameters with no slab present; all other parameters were taken from the results of the fitting of ionization curves in water without slabs present. A visualization of how t_w is determined is shown in Figure 2.5.

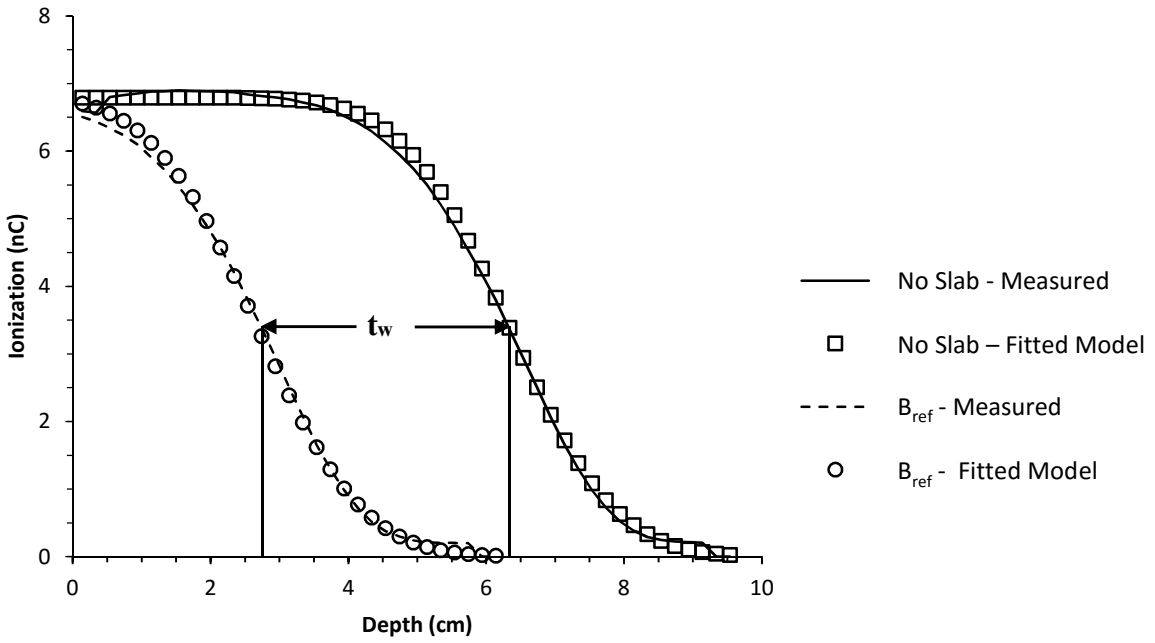

Figure 2.5. A graphic of the range shift for a 12 MeV electron beam with and without B_{ref} placed in the beam. The difference between the two fitted curves at 50% ionization is the measured water equivalent thickness, t_w, for the slab placed in the beamline, as indicated by the vertical lines.

To account for model fitting errors in the extraction of measured t_w values, a correction factor was applied to the measured t_w values determined using both the measured and calculated ionization curves. The purpose of this correction factor is to account for differences between the measured ionization curves and fitted models, minimizing the effect of these deviations on measured t_w values. For each recorded ionization curve, a straight line was fit to the linear distal falloff of the dose distribution for the measured data. The ionization curve-specific correction was calculated as the difference between the 50% ionization depths, R_{50}, for the measured linear fit and the calculated distal falloff (Figure 2.6). The correction for each ionization curve was determined to be positive if the calculated ionization curve under-predicted R_{50}, and negative if the calculated ionization curve over-predicted R_{50}. The correction factor, dR, for each measured t_w was determined using

$$\mathrm{dR} = dR_w + dR_m \tag{2.8}$$

where dR_w is the correction for the ionization curve fit with no slab present and dR_m is the correction for the ionization curve fit with a slab present. dR is then added to the measured t_w values to get the corrected values.

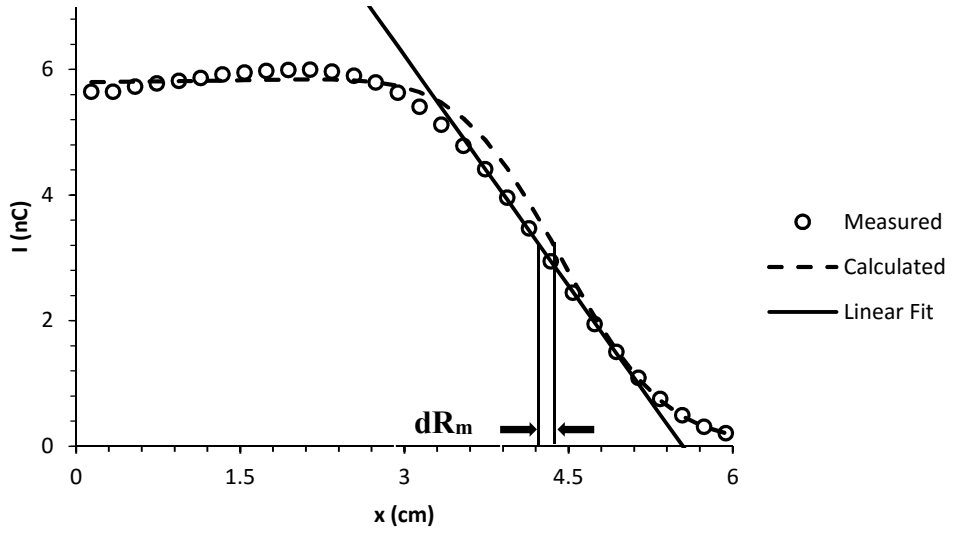

Figure 2.6. A graphic of the model fitting correction for a 12 MeV electron beam incident on the slab $L_{p,\,16.8\%}$. The difference between the R_{50} values for the calculated ionization curve and the fitted distal falloff is the correction for the curve shown. The correction is negative given the model's over-prediction of R_{50} for the measured data.

2.1.4. WET Uncertainty Analysis

To determine the accuracy in the WET measurements, uncertainties were calculated for the predicted t_w values (Section 2.1.1) and the extracted WET values (Section 2.1.3). The uncertainties for the calculated WET were determined using the general equation

$$\delta_q = \sqrt{\left(\frac{\partial q}{\partial x}\delta x\right)^2 + \cdots + \left(\frac{\partial q}{\partial z}\delta z\right)^2} \tag{2.9}$$

for some function $q(x, \dots, z)$, where δ_q is the uncertainty in function q, $\frac{\partial q}{\partial x}$ is the partial derivative of function q with respect to variable x, δx is the uncertainty for variable x, $\frac{\partial q}{\partial z}$ is the partial derivative of function q with respect to variable z, and δz is the uncertainty for variable z (Taylor 1982). The design t_w uncertainty was dependent on the uncertainty in the reference slab thicknesses (± 0.01 mm), the density of the reference materials (± 2 mg/cm^3), and the mass stopping powers (± 0.05 MeV•cm^2/g). The mass density uncertainty for the lung reference material was determined by the ASTM Standard for epoxy resins (2009). Using these values, the maximum uncertainty in the design t_w was calculated as ± 0.2 mm.

The uncertainty in the corrected t_w was determined using

$$\delta_q = \sqrt{(\delta x)^2 + \cdots + (\delta z)^2}, \qquad 2.10$$

for some function $q(x, \dots, z)$, where δx is the uncertainty for variable x and δz is the uncertainty for variable z (Taylor 1982). The two components of the corrected t_w were σ_{dR} (Equation 2.8) and σ_{t_w}. σ_{t_w} was approximated as being equivalent to $\sigma_{c_{dist}}$ because t_w (Equation 2.4) is most sensitive to changes in c_{dist} (Equation 2.6). This approximation ignores Equations 2.5 and 2.7, which exhibit minimal variation between different ionization curves. The uncertainty in c_{dist}, $\sigma_{c_{dist}}$, was determined to be 0.135 where σ_σ and $\sigma_{R_{50}}$ represent the uncertainty in the fitting parameters σ and r_{50}, respectively. These uncertainties were approximated by perturbing the fitting parameter values to get a population sample.

σ_{dR} was determined using Equation 2.10, with the two components σ_{dR_w} and σ_{dR_m} representing the uncertainties in dR_w and dR_m, respectively. σ_{dR_w} and σ_{dR_m} were both

determined by perturbing the fitting parameters for the correction factors as described above. Using the above equations, the uncertainty in the corrected t_w was calculated as ±1 mm.

2.2. Aim 2: Comparison of Printed and Molded Reference Slabs

The goal of this aim was to verify that a reference anthropomorphic phantom section can be printed with the same geometry and range shift properties as a traditional molded phantom section. The working hypothesis for this aim was that the 3D printing system and materials can be configured to provide accurate control of the dimensions and mass density of printed objects of mass density less than 1.14 g/cm^3. This was accomplished by performing absorbed dose measurements from electron beams downstream of the printed and molded reference slabs.

2.2.1. Printed Phantom Design and Fabrication

The phantom section chosen for this experiment was a cranial section of a pediatric anthropomorphic reference phantom (Model 706-C ATOM® Pediatric 10 Year Old Dosimetry Phantom, S/N 706-L1652, CIRS Inc., Norfolk, VA). To design the corresponding printed slab, the pediatric reference phantom head was imaged using a clinical CT scanner (GE Lightspeed RT16, S/N 1255068, GE Healthcare, Little Chalfont, Buckinghamshire, United Kingdom) located at MBPCC. The phantom was aligned on the scanner couch following the standard of care used for patients. The phantom was aligned such that the scan origin was positioned at the seam between two sections of the phantom head to allow for better delineation of the molded phantom sections. A 40 cm head scan was taken using 2.5 mm slice thickness, 120 kV tube potential, and 400 mA tube current. The image set was then exported to the radiation therapy treatment planning system (Pinnacle^3 Treatment Planning System Version 9.8, Philips Healthcare, Andover, MA).

In the treatment planning system (TPS), the exterior geometry of the desired phantom section was contoured to create the surface of the printed slab structure (Figure 2.7). The high density (bone) heterogeneities present in the CT image were overridden to have the same HU value as the soft tissue because the printer could not print objects with mass density greater than 1.14 g/cm^3. The 2.5 cm thick printed slab was subdivided into five separate regions of interest (ROIs) to facilitate printing. Each ROI corresponded to a subsection thickness of 0.5 cm. The contoured ROIs were then extracted from the TPS and imported into a file stitching program developed in house.

The stitching program utilized the 3D coordinates of the contours to develop a watertight solid with the same geometry as the contoured subsection. Three-dimensional structures were generated from the ROI data by stitching together the contours of adjoining slices to form a surface mesh. The stitching was accomplished by forming triangular facets using the three coordinates of each contour. The triangular stitching was done in a logical progression, stitching each coordinate to the nearest point. The surface orientation was determined by the normal vector of the triangle surface. An exterior pointing vector indicated an outer surface. Likewise, an interior pointing vector indicated an interior surface. Any errors created using this process were corrected by reassigning the stitching point(s). The completed surface structures were then converted to an STL file using 3D structure rendering program (Repetier-Host, Hot-World GmbH & Co. KG, Willich, Germany).

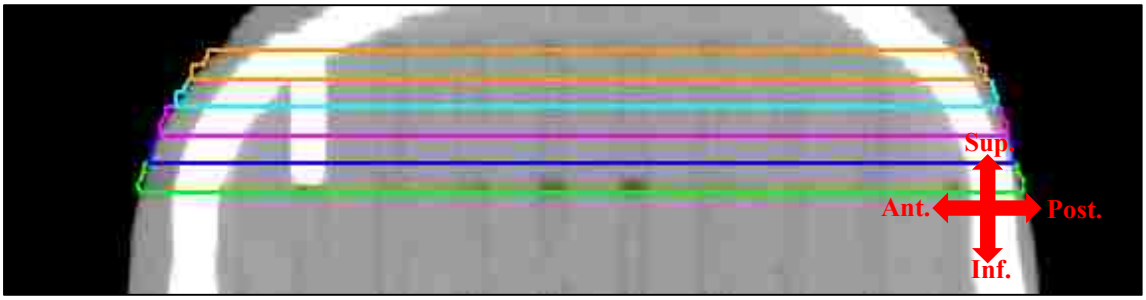

Figure 2.7. A sagittal image of the ROIs used to design the printed slab. Each different-colored contour represents a different structure of the printed phantom section design. Designing and printing the phantom in multiple ROIs reduced the probability of errors in printing the structures.

The STL ROIs were printed using the print settings specified in Section 2.1.1. After printing, the edges were smoothed with a rasp to provide better surface contact between printed slices. The printed slab was then compressed together using tape to minimize any air gaps between the printed slices. Images of the printed and molded slabs are shown in Figure 2.8.

Figure 2.8. Printed and molded anthropomorphic slabs. The molded slab (right) contains several heterogeneities that were not reproduced in the printed slab (left), including bone, the section connector pins on the superior surface, and the connector slots on the inferior surface (not shown).

2.2.2. Penetration Range Measurements

The penetration range measurements were performed at MBPCC with standard dose measurement methods using the same electron linear accelerator described in Section 2.1.2. All

doses were recorded using radiochromic film (EBT3 Gafchromic Film, Ashland Inc., Covington KY, Lot #06051403). Prior to performing measurements, film calibration irradiations were performed for electron energies of 6, 9, 12, 16, and 20 MeV. Each film sheet was cut into 6.4 x 10.2 cm^2 sections for individual calibration irradiations. All calibration irradiations for a single energy were recorded using the same film sheet to minimize any intra-batch variability in the calibration curve. At each electron energy, calibration doses of 0, 50, 100, 150, 200, 250, and 300 MU were delivered to individual film sections at a dose rate of 600 MU per minute. The irradiation setup utilized a 6x6 cm electron cone and a 4x4 cm lead alloy insert, with all measurements performed at 100 cm SSD. Film sections were placed at the respective d_{max} in water equivalent plastic for each energy, with 10 cm of water equivalent plastic serving as a media for backscatter. The value d_{max} is the depth at which the maximum dose was delivered. For 6, 9, 12, 16, and 20 MeV electron beams, these values for the calibration field size are 1.5, 2.0, 2.4, 2.0, and 1.2 cm, respectively. The linac was calibrated such that 1 MU delivered in water is equivalent to 1 cGy of absorbed dose at d_{max}, therefore making the MU calibration quantities listed above equal to the calibration doses in cGy.

The electron beam range measurements were performed at 100 cm SSD, with 10 cm of water-substitute plastic (Plastic Water, CIRS Inc., Norfolk, VA) used to provide electron backscatter. A 20x20 cm electron cone was used to provide a large enough field size to irradiate the entire slab. For each irradiation a sheet of film was placed between the slab and the water equivalent plastic, as shown in Figure 2.8. For 6, 9, 12, 16, and 20 MeV electron energies, irradiations of 200 MU each were delivered to both the molded and printed slabs. Two film irradiations were performed for each slab at each energy.

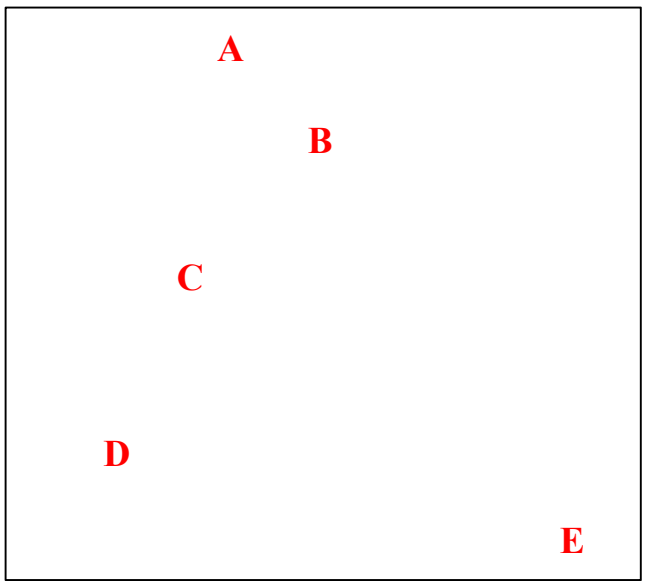

Figure 2.9. The setup used for performing electron beam penetration range measurements with the slabs. Pictured is the printed reference slab, which is oriented along the central axis of the perpendicular beam and positioned atop the film sheet. The setup includes (A) electron beam cone, (B) printed slab, (C) radiochromic film, (D) water-substitute plastic, and (E) treatment couch.

2.2.3. Dosimetric Analysis

The irradiated films were allowed to sit for 24 to 48 hours after exposure to permit any further changes in color density prior to their digitization (Niroomand-Rad et al. 1998). All films were digitized using a flatbed scanner (Expression 10000 XL, Epson America, Inc., Long Beach, CA). To avoid any effects from changes in light intensity of the scanner lamp, five warmup scans were performed to stabilize the light output as recommended by Paelinck et al. (2007) . Scans were performed following the film manufacturer recommendations, 48-bit color image with 72 dpi resolution and no color correction. Each film was aligned lengthwise with the scanner bed and oriented to match the irradiation conditions, then scanned using the red channel as recommended by the manufacturer for therapeutic dose ranges.

The dosimetric analysis of the irradiated films was performed using commercial quality assurance software (RIT Radiation Therapy QA and Diagnostic Imaging QC Software, Radiation Imaging Technology, Colorado Springs, CO). All of the film scan files were imported and processed using a red channel filter, which provides the highest dose sensitivity for range of doses utilized in this study. Film calibration curves were established for each energy from the energy-specific calibration film. This was accomplished by importing the calibration film image and designating a 2 x 2 cm^2 ROI in the center of each irradiation. These ROIs were then assigned their corresponding dose value to create the calibration points.

The measured 2D dose distributions behind the printed and molded reference slab irradiations were compared using gamma index analysis. The gamma index analysis formalism used in this work was described by Low et al. (1998). Gamma index analysis is an analytical tool that relies on dose difference (DD) and distance to agreement (DTA) of points to compare measured and calculated dose distributions. Similarly, a value of less than or equal to one indicates a pass for a specific point calculation. These two criteria are used to calculate the gamma index, $\Gamma\,(r_m, r_c)$,

$$\Gamma\,(r_m, r_c) = \sqrt{\frac{r^2(r_m, r_c)}{\Delta d_M^2} + \frac{\delta^2(r_m, r_c)}{\Delta D_M^2}}, \tag{2.10}$$

where r_m and r_c are the locations of the measured and calculated dose values, respectively. The first component of the equation under the radical is concerned with DTA. The metric r is determined as the absolute value of the difference between the points of measurement and calculation, and Δd_M is the DTA criterion. Likewise, δ is the DD between the points of measurement and calculation, and ΔD_M is the DD criterion. Using this equation, a point of measurement will fail in comparison to the point of calculation if it does not fall within the

criteria of Δd_M or δ. A gamma index value greater than one indicates the failure of a specific measured data point. Similarly, a value of less than or equal to one indicates a pass for a specific measured data point. A graphical representation of two dimensional gamma index acceptance criteria is shown in Figure 2.10.

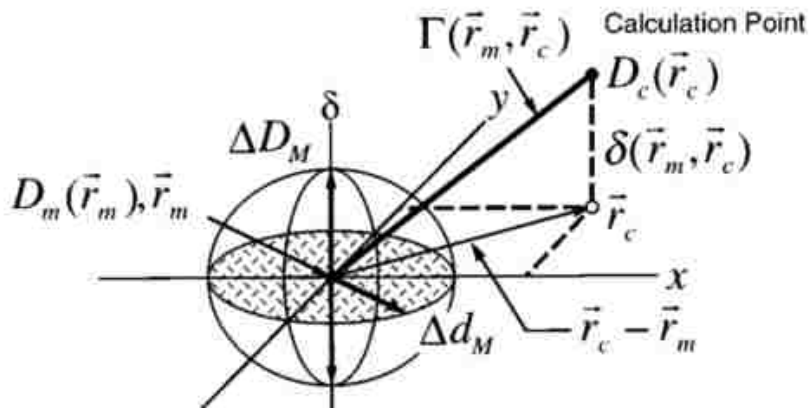

Figure 2.10. A diagram of the gamma index analysis formalism. Image adapted from Low et al. (1998).

For this study, the molded slab doses served as the reference for gamma analysis. At each electron beam energy, one molded slab image was imported to serve as the reference image and one printed slab image was imported to serve as the test image. The calibration curve for the chosen energy was applied to both images, which were then registered to one another using five automatically placed registration points. The measured doses were normalized to the reference image's centroid dose.

Because the bone heterogeneities in the molded slab were not present in the printed slab, three different regions of interest were used for the gamma index analyses (Figure 2.11). These ROIs examined the entire slab image, a region of bone-soft tissue interface, and a homogeneous brain tissue region. The full slab ROI (ROI 1) had dimensions of 17.6 x 15.5 cm^2 and was centered over the full image. The bone-tissue interface ROI (ROI 2) had dimensions of 3.0 x 5.7

cm^2 and was centered on the posterior central region of the image. The homogeneous brain ROI (ROI 3) had dimensions 5.0 x 6.0 cm^2, and was positioned in the center of the brain region, just anterior of the connector pins. Each ROI provided different insights into the dosimetric performance of the printed slab in comparison to the molded slab. For each region the gamma analysis pass rate was determined using the widely used clinical criteria of 3% DD and 3 mm DTA.

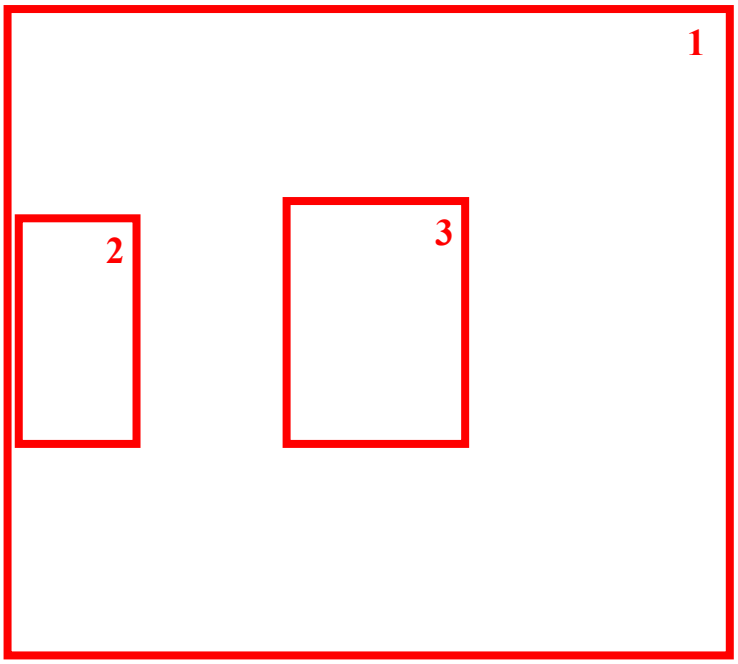

Figure 2.11. The regions of interest used for the gamma index analyses of the molded and printed slabs. The red bounding boxes indicate the three ROIs used in the comparison of the molded and printed slabs. ROIs 1, 2, and 3 examine the entire image, a region of bone-tissue interface, and a homogeneous brain tissue region, respectively.

2.3. Aim 3: Comparison of Printed Personalized and Molded Reference Phantoms

The goal of this aim was to determine the dosimetric accuracy that a personalized printed phantom can achieve for assessing patient-specific electron beam radiotherapy plans. This was accomplished by designing and printing a personalized head phantom based on patient CT image data, then comparing the dose distributions in personalized and reference phantoms. The

dosimetric analysis was accomplished by performing electron beam dose calculations for the molded reference phantom, the printed personalized phantom, and the patient, with the latter serving as the best estimate of the true dose distributions.

2.3.1. Phantom Design and Fabrication

To create the personalized phantom, a patient CT image set was selected to serve as the design basis. The patient selected for this study had a partial nose amputation due to prior disease in the nasopharyngeal region. This resulted in the patient having atypical internal and external anatomy, which presented a severe test of reference phantoms for personalized electron beam radiotherapy treatments.

The patient images were imported into the TPS and selected cranial anatomy was contoured. The anatomical region for creating the phantom extended from just superior of the frontal sinus to the midpoint of the oral cavity, and posterior to the auditory canal (Figure 2.12). The exterior surface was contoured using the automated contouring feature in the TPS. The patient positioning mask and bolus were manually excluded. Due to limitations in printing capabilities, the phantom was designed such that all tissues were designated as either plastic or air. This was accomplished by using locally drawn ROIs to determine the density of anatomical regions. If the average CT number of a ROI was greater than 900 HU, it was determined to be plastic. A CT number of less than 900 HU was designated as air. Using this method, the interior heterogeneities of the patient were delineated to create the printed phantom geometry.

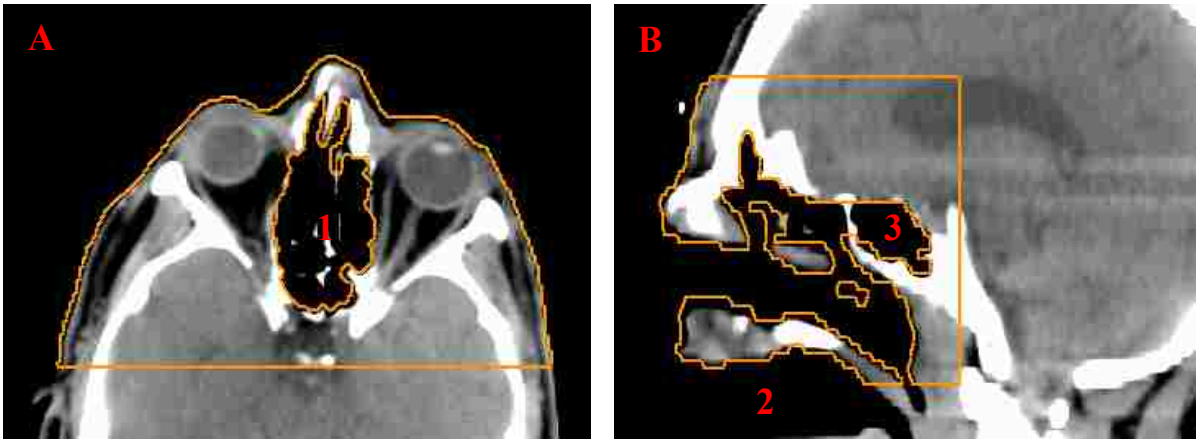

Figure 2.12 Transverse (A) and sagittal (B) views of the patient anatomy and printed phantom design at isocenter. The orange line represents the phantom exterior surface. The printed phantom design includes the (1) ethmoidal sinus, (2) sphenoidal sinus, and (3) oral cavity.

The anatomical contours were extracted from the TPS and stitched together utilizing the same methodology described in Section 2.2.1. The phantom was divided into 12 subsections to allow for easier printing. Ten sections had a thickness of 0.75 cm and two sections had thicknesses of 0.25 and 1.00 cm, respectively. Section thickness were selected to enhance accurate printing of the heterogeneities. This is because the temperature gradient across solid print structures can cause warping of the structure. The degree of warping increases with the thickness of the printed section. All sections were graphically rendered and reoriented if necessary to reduce the risk of print errors from the filament deposition process. The phantom sections were printed using the print settings previously described in Section 2.1.1. The finalized printed phantom is shown in Figure 2.13.

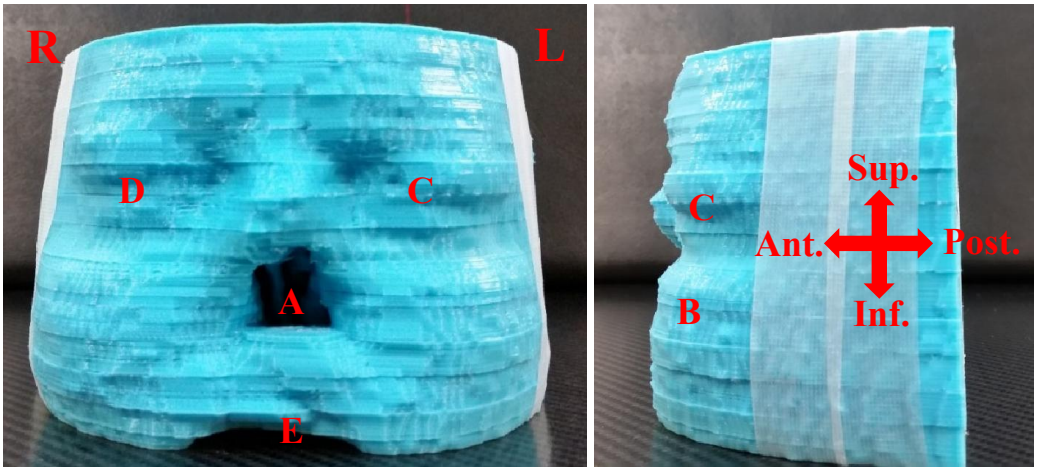

Figure 2.13. Anterior (left) and lateral (right) views of the personalized printed phantom. The printed phantom anatomical features include (A) the nose amputation cavity, (B) an example of abnormal surface anatomy, (C) left eye, (D) right eye, and (E) the oral cavity. Visual inspection of the phantom shows minor surface errors from the phantom design and printing process on the phantom surface. Additional print errors were seen in the internal cavities (not shown).

2.3.2. Electron Beam Dose Calculations

Electron beam radiotherapy dose calculations were used to compare both the printed personalized head phantom and the molded reference head phantom to the patient for radiological equivalency. For this work it was assumed that there no errors in the TPS pencil beam algorithm. The dose calculations were performed on the patient CT image data.

A 6 x 6 cm^2 electron beam was positioned perpendicular to the patient's nasopharyngeal region (Figure 2.13). The central axis of the beam was aligned with the isocenter of the patient, which was had a lateral position of 1.49 cm, an anterior-posterior position of 17 cm, and a superior-inferior position of 3.1 cm. The prescription used for all simulated irradiations was 200 cGy per fraction for 25 fractions, normalized to a dose calculation point at a depth of 0.5 cm posterior to isocenter. Using these parameters, separate dose calculations were created for electron beam energies of 6, 9, 12, 16, and 20 MeV.

Because of the density heterogeneities that were present in the patient but not the printed phantom, the absolute dose was recalculated with the patient's tissue density overridden to quantify the impact of these heterogeneities on the study. The densities used were 1.00 and 1.60 g/cm^3 to replicate water and bone, respectively. These values were selected because water is the clinical standard as a surrogate for human tissue, and the bone density is the recommended value stated in ICRP Report 23 for reference male bone density (Snyder et al. 1975, Almond et al. 1999). The exact choice of density was arbitrary due to the gamma index comparison not being sensitive to this test. Rather, this facilitated a direct comparison of the results for the electron beam dose calculations in both the patient and personalized phantom.

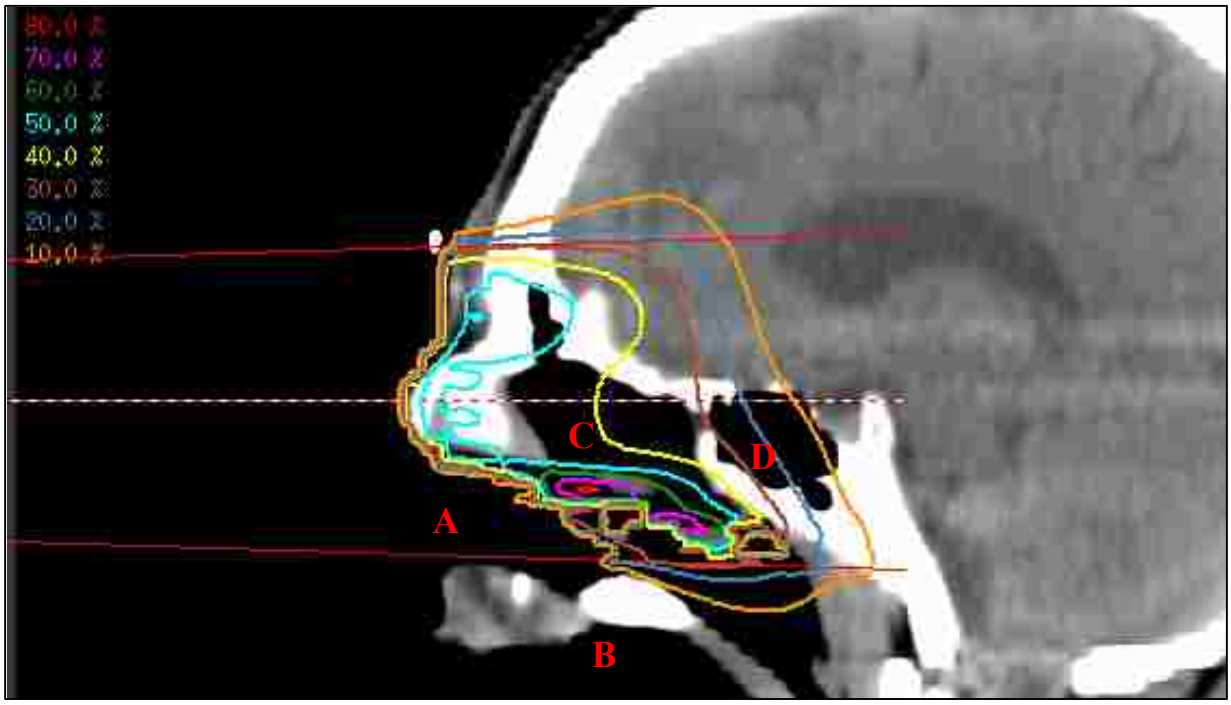

Figure 2.14. A sagittal view of the dose calculations for a 12 MeV electron beam incident on the patient. The isodose lines show the relative dose distributions in the patient for the irradiation simulation. (A) indicates the region where the nose was amputated, (B) is the upper oral cavity, (C) is the ethmoidal sinus, and (D) is the sphenoidal sinus.

The electron beams designed using the patient CT data, described above, were copied and inserted into treatment plans containing the personalized and reference phantoms. The personalized phantom and reference phantom heads were imaged using the clinical CT scanner and scan settings described in Section 2.2.1, then imported into the TPS. The orientation of the beam with respect to the phantom was determined by registering the phantom image set to the patient image set using image fusion tools within the TPS (Figure 2.15). The accuracy of the image registration was verified by a clinical medical physicist. The image registration parameters for both the personalized and reference phantoms are listed in Table 2.5. After registration was completed, the isocenter, dose calculation point, beam position, and dose grid were all shifted according to the registration parameters specific to each phantom. The dose calculations were then performed for both phantoms.

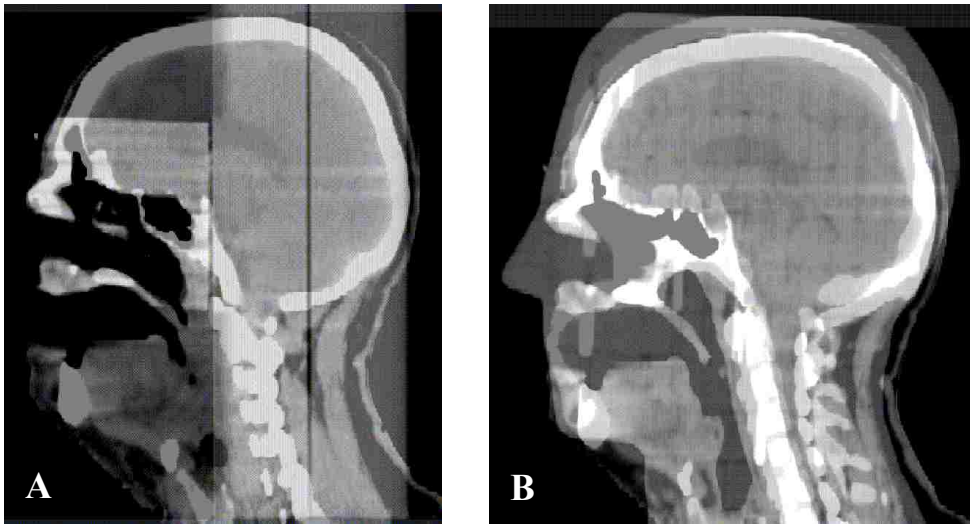

Figure 2.15. Sagittal views of the image fusions of the patient to the personalized and reference phantoms. The printed phantom (A) showed much better visual agreement with the patient imaging data than the reference phantom (B) due to its geometric agreement.

For the patient and both phantoms, the dose distributions for each beam energy were extracted from the TPS as an individual Digital Imaging and COmmunications in Medicine (DICOM) file set. These files were analyzed using gamma index analysis software, as described in Section 2.3.3.

Table 2.5. Image registration parameters for the patient, personalized printed phantom, and molded reference phantom.

	Translation (mm)		Rotation (°)	
Direction	Personalized Phantom	Reference Phantom	Personalized Phantom	Reference Phantom
ANT-POST	-16.6	-01.6	0	0
SUP-INF	-85.6	26.8	0	0
R-L	-28.6	-48.6	0	4

2.3.3. Dosimetric Comparison

The 2D dose distributions in the patient were compared with those in the phantoms using the gamma index analysis formalism (described in Section 2.2.3). The analyses were performed using commercial quality assurance software (SNC Patient, Sun Nuclear Corporation, Melbourne, FL). The dose distributions were imported into the QA software, with the patient data serving as the reference data. For each comparison, the patient isocenter was realigned during file import process using the parameters listed in Table 2.6. The number of points passing and failing were determined using a criteria of 3% local DD or 3 mm DTA, with a minimum dose threshold of 10%. The minimum dose threshold limits the gamma index calculations to only dose points that are above 10% of the prescribed dose, ignoring everything below this threshold percentage. This eliminates doses that aren't of concern for the target volume dose coverage.

Table 2.6. Patient isocenter translation parameters. The listed parameters were the recorded translation values from the image set registration described in Section 2.3.2, and were used in matching the patient and phantom data sets for gamma index analyses.

	Translation (mm)			Rotation (°)		
Direction	Patient	Personalized Phantom	Reference Phantom	Patient	Personalized Phantom	Reference Phantom
ANT-POST	0	-16.6	-01.6	0	0	0
SUP-INF	0	-85.6	26.8	0	0	0
R-L	0	-28.6	-48.6	0	0	4

Gamma index analyses were performed for 6, 9, 12, 16, and 20 MeV electron beam energies. Each data set consisted of 100 slices at separations of 1 mm. To perform the gamma analyses, both data sets were adjusted to display transverse dose distributions and the maximum superior slice position. Gamma indices were calculated at every 2 mm depth for the entirety of the data sets, with the number of passing and failing points recorded for each depth. The pass rate for each comparison was determined as the number of passing points over the total number of points.

Chapter 3: Results

The results of range shifting properties of phantom materials and fabrication techniques are presented in Section 3.1, the comparison of printed and molded slabs with matched geometry in Section 3.2, and the comparison of the printed personalized head phantom to the molded reference phantom for electron beam dose calculations in Section 3.3.

3.1. Aim 1: Comparison of Phantom Materials and Fabrication Techniques

In this aim we calculated the WET for selected reference materials, then designed and printed slabs with the same calculated WET. A series of slabs with variable layer height and infill density were also printed to determine the impact these print settings have on the average mass density of printed objects.

3.1.1. Water Equivalent Thickness Calculations

Table 3.1 lists the values of the WET calculated using the formalisms from Zhang et al. (2010) and IAEA Technical Report Series 398 (2000). Another method for comparing WET values is the water equivalent ratio (WER). WER is the ratio

$$WER = {}^{t_w}/_{t_m} = \frac{\rho_w\left(\overline{\frac{dE}{\rho dx}}\right)_w}{\rho_m\left(\overline{\frac{dE}{\rho dx}}\right)_m}, \quad 3.1$$

, where t_w is the WET for a given material, t_m is the thickness of a given material, ρ_w is the density of water, ρ_m is the density of the material, $\left(\overline{\frac{dE}{\rho dx}}\right)_w$ is the average mass stopping power in water, and $\left(\overline{\frac{dE}{\rho dx}}\right)_m$ is the average mass stopping power in the material. This method provides another method of examining ratios of mass densities and mass stopping powers, which are needed to calculate WET (Zhang and Newhauser 2009). The analogous WER equation for the IAEA formalism is

$$WER = {}^{z_w}/_{z_{pl}} = \frac{\rho_w}{\rho_{pl}} * \frac{R_{CSDA,\,w}}{R_{CSDA,\,pl}}, \qquad 3.2$$

Where ${}^{z_w}/_{z_{pl}}$ is the ratio of WET to material thickness for a given material, ρ_w is the density of water, ρ_m is the density of the material, $R_{CSDA,\,w}$ is the CSDA range in water, and $R_{CSDA,\,m}$ is the CSDA range in the material. This method utilizes CSDA ranges in place of the mass stopping powers as seen in Equation 3.1. A comparison of the water equivalent ratios is shown for both formalisms in Figure 3.1.

Table 3.1. The calculated WET values, denoted by t_w (see Equation 2.1), using formalisms from Zhang and Newhauser (2009) and IAEA TRS 398 (2000).

Electron Beam Energy (MeV)	t_w (mm)					
	Reference Lung			Reference Bone		
	Eq. 2.1	Eq. 2.2	% Diff.	Eq. 2.1	Eq. 2.2	% Diff.
6	5.341	5.293	0.900	33.979	33.967	0.036
9	5.334	5.308	0.499	33.986	33.967	0.056
12	5.324	5.313	0.198	33.970	33.975	0.014
16	5.304	5.314	0.181	33.960	33.974	0.041
20	5.289	5.310	0.414	33.946	33.970	0.070

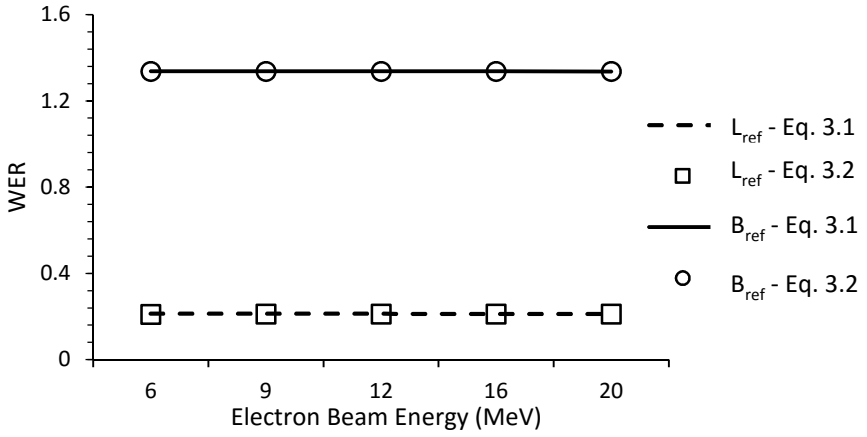

Figure 3.1. Comparison of the WER values in Equations 3.1 and 3.2. The methods of Zhang and Newhauser (2009) and the IAEA (2000) are in good agreement.

3.1.2. Printed Slab Properties

The physical characteristics of the printed slabs (see Table 2.3) are listed in Table 3.2. For the $L_{p,\ 16.8\%}$ slab, the mass and volume of the sidewalls was removed from the density calculation following the method described in Section 2.1.1. The average mass density of the printed slabs revealed that structures printed with 100% infill density had a mass density less than that of the printer filament because of small void spaces introduced by the printing process. This was qualitatively confirmed with an imaging study that examined a solid printed slab with a microtomograph (SkyScan 1074 Portable X-Ray Microtomograph, Micro Photonics Inc., Allentown, PA). The images reveal density variations from the layering process (Figure 3.2).

Table 3.2. The measured dimensions, mass, and mass density for the printed slab phantoms used in the range shift measurements. The estimated densities are the manufacturer stated values for each reference material.

Slab	t_m (mm)	Mass (g)	Vol. (cm^3)	Density (g/cm^3)			ρt_m (g/cm^2)		
				Meas.	Est.	Diff. (%)	Meas.	Est.	Diff. (%)
$L_{p,\ 100\%}$	4.49	32.6	28.8	1.134	1.24	9.35	0.509	0.564	10.77
$L_{p,\ 16.8\%}$	24.81	53.0	159.2	0.197	0.21	6.60	0.489	0.525	7.42
$B_{p,\ 100\%}$	28.80	210.7	183.7	1.147	1.24	8.11	3.303	3.605	9.13

It is important to note that not all of the measured dimensions for the printed slabs fell within the 0.2 mm printer accuracy stated by the manufacturer. These dimensional printing errors (see Table 2.3) could be due to slight deviations in printer assembly and alignment, such as the assembly of the extruder guidance track or the leveling of the print bed. These deviations have the potential to increase range errors in range shift measurements.

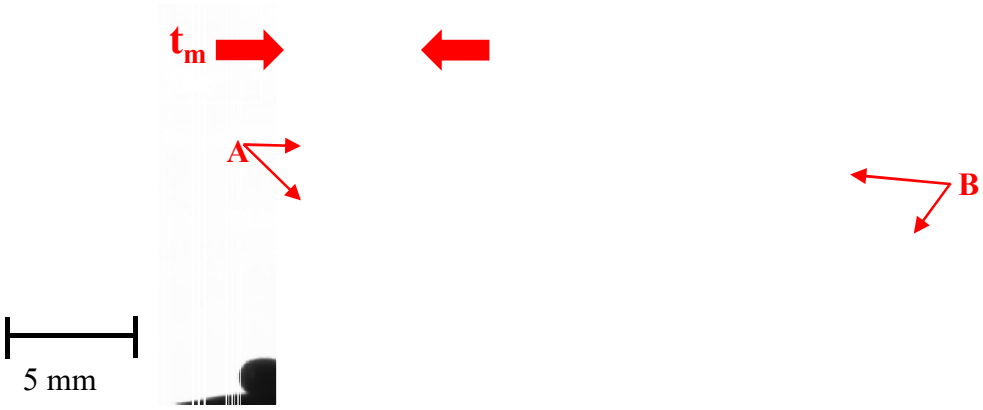

Figure 3.2. MicroCT images of a printed slab. The left profile shows the layer spacing (A) and how density variations at depth are correlated with structure and layer height. The right profile shows the air gaps in the structure (B) that are a result of the infill pattern.

The study of how varying the printing parameters for layer height and infill density affect a printed object's average mass density are listed in Table 3.3 and plotted in Figure 3.3. In review, these two print settings were selected for the variables of this experiment as they have the greatest impact on the total mass of material used in creating 3D printed objects (see Table 2.4). The observed densities reflect the reduction in the average densities seen in Table 3.2. Varying the layer height shows very little influence on the average mass density. The significance of this finding is that printing at a greater layer height allows for faster print times without a significant variation in printed material density. The difference in predicted and observed average mass densities for different infill density settings shows a consistent deviation, which can be accounted for in future printed structure design. It is important to note that the results of this experiment are only for the grid infill pattern as the other infill patterns available were not studied.

Table 3.3. The predicted and observed average mass density for four slabs printed with variable settings for layer height and infill density.

Slab	Mass Density			
-	Predicted (g/cm^3)	Observed (g/cm^3)	P-O (mg/cm^3)	(P-O)/O (%)
T1	0.625	0.539	85.7	15.9
T2	0.625	0.557	67.9	12.2
T3	1.24	1.161	88.7	7.6
T4	0.124	0.061	63.7	103.8

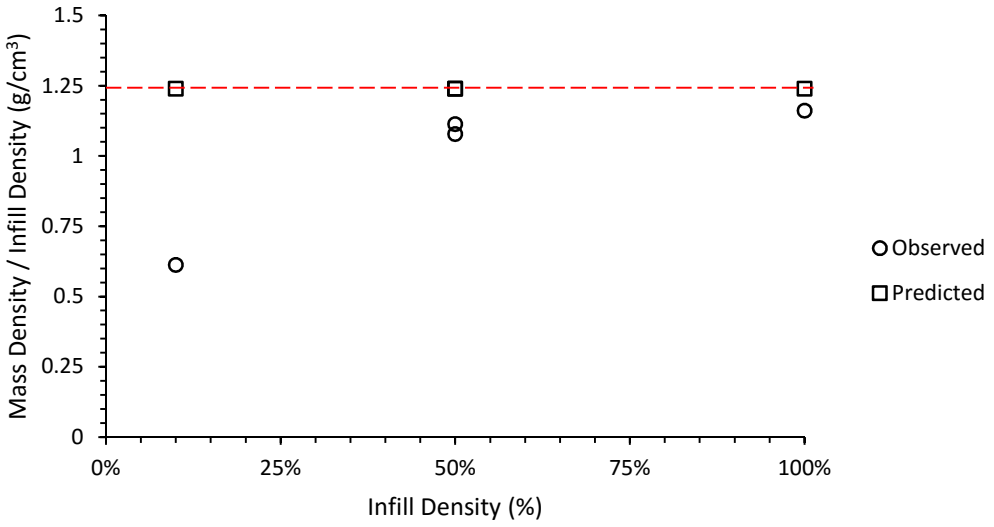

Figure 3.3. Comparison of the predicted (squares) and observed (circles) average mass densities for four slabs printed with variable settings for layer height and infill density. The mass densities are normalized by the infill density. The red line indicates the filament mass density.

3.1.3. Water Equivalent Thicknesses

The uncorrected WET values of the lung slabs are listed in Table 3.4 along with the design and adjusted design t_w values. The uncorrected WET values of the bone slabs are listed in Table 3.5 along with the design and adjusted design t_w values. The design t_w values listed are the theoretical WET values determined using Equation 2.1 and listed in Table 2.1, which were used

in designing the printed slabs. The adjusted design t_w was introduced because the measured t_w values did not meet the design t_w values for either reference slab. This new value is the calculated WET for the printed slabs (see Equation 2.1) multiplied by the ratio of the measured t_m for the printed slab (Table 3.2) to the design t_m of the printed slab (Table 2.3).

Table 3.4. The designed, adjusted design, and uncorrected measured t_w values for the lung slabs.

Electron Beam Energy (MeV)	t_w (mm)					
	Design t_w (Eq. 2.1)	Adj. Design t_w ($L_{p,\ 100\%}$)	Adj. Design t_w ($L_{p,\ 16.8\%}$)	L_{ref}	$L_{p,\ 100\%}$	$L_{p,\ 16.8\%}$
6	5.341	5.180	4.875	6.238	3.949	3.595
9	5.334	5.183	4.877	6.341	4.037	3.196
12	5.324	5.182	4.876	6.449	4.038	3.657
16	5.304	5.174	4.870	6.962	4.893	5.075
20	5.289	5.172	4.867	6.760	5.028	4.997

Table 3.5. The designed, adjusted design, and uncorrected measured t_w values for the bone slabs.

Electron Beam Energy (MeV)	t_w (mm)			
	Design t_w (Eq. 2.1)	Adj. Design t_w ($B_{p,\ 100\%}$)	B_{ref}	$B_{p,\ 100\%}$
6	33.979	33.322	-	-
9	33.986	33.339	-	-
12	33.970	33.332	35.280	32.316
16	33.960	33.287	36.623	33.060
20	33.946	33.270	36.471	32.986

Table 3.6 lists the model fitting correction factors for errors in extracting t_w. As described in Section 2.1.3 and visualized in Figure 2.6, the purpose of these correction factors was to account for differences between the measured ionization curves and fitted models, minimizing

the effect of these deviations on measured WET values. The sign of the individual components of the correction factors (Equation 2.8) was determined by whether the model over- or under-predicted the measured data at the 50% ionization depth, R_{50}.

Table 3.6. The model fitting correction factor values, dR, for the measured ionization curves.

Electron Beam Energy (MeV)	dR (mm)					
	No Slab	L_{ref}	$L_{p,\ 100\%}$	$L_{p,\ 16.8\%}$	B_{ref}	$B_{p,\ 100\%}$
6	-0.236	0.354	0.284	0.998	-	-
9	-0.136	0.381	0.209	1.378	-	-
12	-0.035	-0.171	0.259	1.394	0.058	0.058
16	-0.128	-0.370	-0.140	0.299	-0.408	-0.371
20	0.114	-0.478	-0.234	0.039	-0.639	-0.381

Figure 3.4 shows the uncorrected and corrected t_w values for L_{ref} and $L_{p,\ 16.8\%}$. $L_{p,\ 100\%}$ was omitted from the figure for clarity. Figure 3.5 shows the uncorrected and corrected t_w values for the bone slabs. The corrected t_w values for all printed slabs show a weak energy dependence that ranges between 0.04 and 0.07 mm/MeV which differs from the theoretical WET values determined using Equation 2.1, whose energy dependencies are -0.004 mm/MeV for L_{ref} and -0.001 mm/MeV for B_{ref}. This energy dependence is insignificant in the determination of range shifting properties for reference and printed slabs, and is believed to be a result of the measurement techniques used.

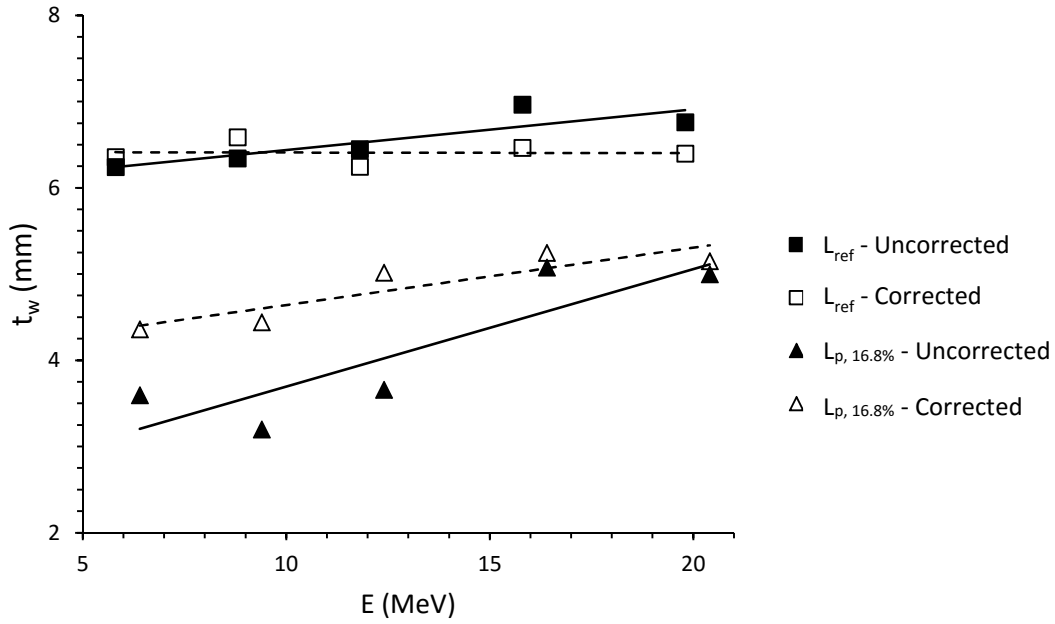

Figure 3.4. Uncorrected (closed) and corrected (open) measured water equivalent thicknesses, t_w, for L_{ref} and $L_{p,\ 16.8\%}$. The trendlines are eye guides for the uncorrected (solid line) and corrected (dashed line) data points. The data points are slightly offset at each energy and $L_{p,\ 100\%}$ is omitted from the plot for visual clarity.

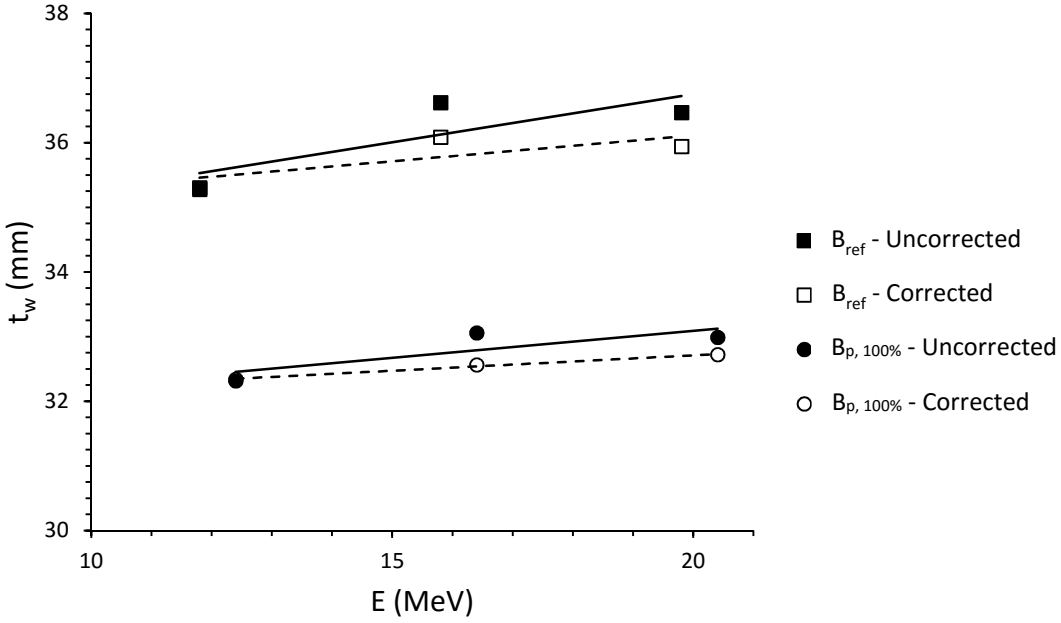

Figure 3.5. Uncorrected (closed) and corrected (open) measured water equivalent thicknesses, t_w, for B_{ref} and $B_{p,\ 100\%}$. The trendlines are eye guides for the uncorrected (solid line) and corrected (dashed line) data points. The data points are slightly offset at each energy for visual clarity.

Table 3.7 lists the corrected measured t_w values for the lung slabs and the design and adjusted design t_w values referenced from Table 3.4. Figure 3.6 plots the designed and corrected measured t_w values for the lung slabs. While both $L_{p,\,100\%}$ and $L_{p,\,16.8\%}$ fell short of the design goals, they displayed similar measured t_w despite their different properties (Table 2.3).

Table 3.7. The designed, adjusted design, and corrected measured t_w values for the lung slabs.

Electron Beam Energy (MeV)	t_w (mm)					
	Design t_w (Eq. 2.1)	Adj. Design t_w ($L_{p,\,100\%}$)	Adj. Design t_w ($L_{p,\,16.8\%}$)	L_{ref}	$L_{p,\,100\%}$	$L_{p,\,16.8\%}$
6	5.341	5.180	4.875	6.356	3.996	4.357
9	5.334	5.183	4.877	6.587	4.109	4.439
12	5.324	5.182	4.876	6.243	4.263	5.016
16	5.304	5.174	4.870	6.464	4.625	5.246
20	5.289	5.172	4.867	6.395	4.908	5.149

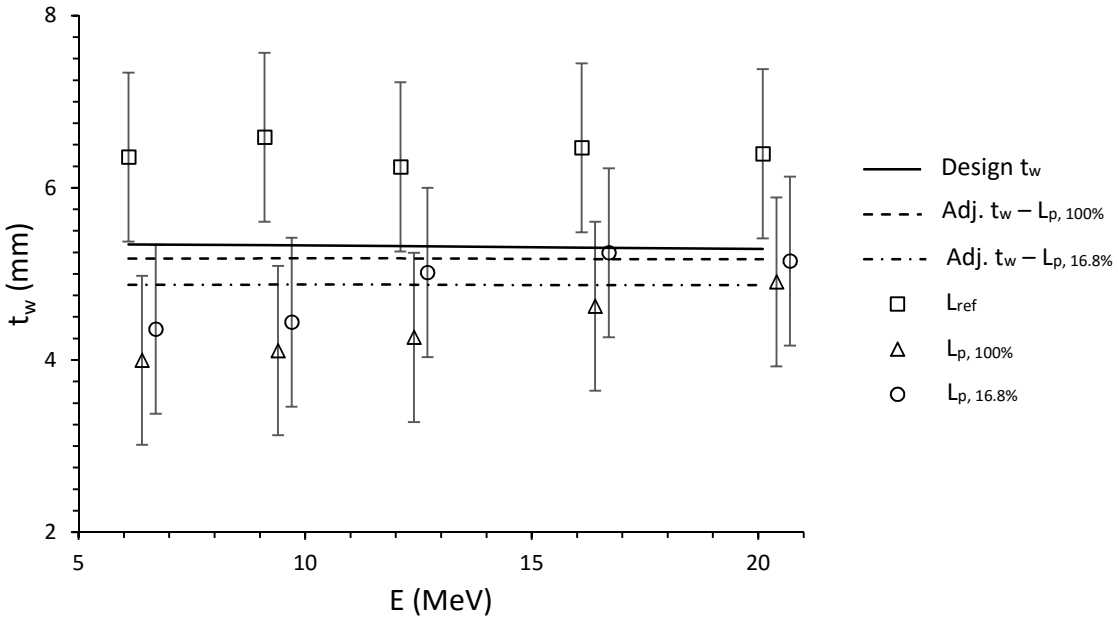

Figure 3.6. Comparison of the theoretical (lines) and corrected measured (points) water equivalent thicknesses, t_w, for the reference and printed lung slabs. The error bars shown were determined in Section 2.1.4. The data points are slightly offset at each energy for visual clarity.

Table 3.8 lists the corrected measured t_w values for the bone slabs and the design and adjusted design t_w values referenced from Table 3.4. Figure 3.7 plots the designed and corrected measured t_w values for the bone slabs.

Table 3.8. The designed, adjusted design, and corrected measured t_w values for the bone slabs.

Electron Beam Energy (MeV)	t_w (mm)			
	Design t_w (Eq. 2.1)	Adj. Design t_w ($B_{p,\,100\%}$)	B_{ref}	$B_{p,\,100\%}$
6	33.979	33.322	-	-
9	33.986	33.339	-	-
12	33.970	33.332	35.304	32.339
16	33.960	33.287	36.087	32.560
20	33.946	33.270	35.945	32.719

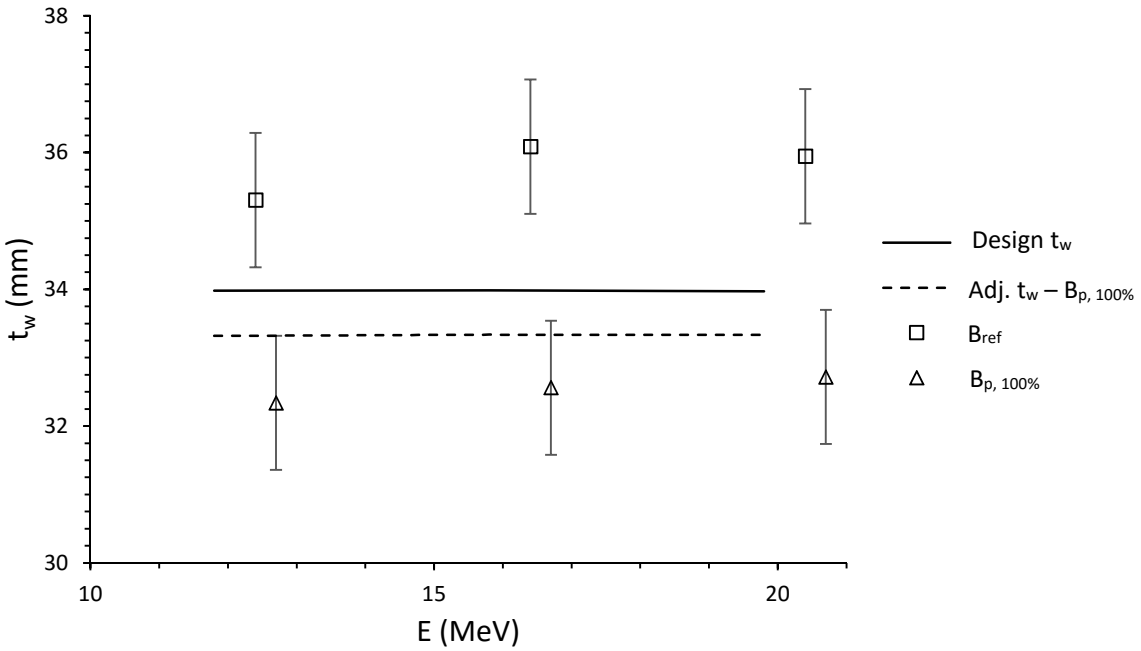

Figure 3.7. Comparison of the theoretical (lines) and corrected measured (points) water equivalent thicknesses, t_w, for the reference and printed bone slabs. The error bars shown were determined in Section 2.1.4. The data points are slightly offset at each energy for visual clarity.

For the lung t_w values, the design, adjusted design, and measured values mostly agreed within a 2 mm margin. The disagreement between the predicted and measured t_w values for the printed slabs is because of the differences between the estimated and measured mass thicknesses for the printed slabs (Table 3.2). The bone design, adjusted design, and measured t_w values reflect this conclusion as well, albeit within a 4 mm margin. Given the known differences between the design and measured mass thicknesses for the printed slabs, the printed slab t_w values for the lung and bone slabs are acceptable.

Section 3.1.2 showed that varying the layer height for printed slabs did not have a significant impact on the average mass density of the printed slabs. The measured mass density of the printed slabs showed a consistent reduction in comparison to the predicted mass density (Figure 3.3) which can be accounted for in future studies. The printed slabs exhibited the same radiological attenuation properties (within 2 mm) as the reference slabs that represent the range of densities in reference anthropomorphic phantoms (Section 3.1.3). For $L_{p,\,16.8\%}$, we were able to mimic the physical and radiological thickness for reference lung by varying the infill density of the printed slab. As stated above, the energy dependence seen in the measured t_w for the printed slabs is insignificant for the range shifting properties of the slabs and is believed to be a result of the measurement techniques used.

3.2. Aim 2: Dosimetric Comparison of Printed and Molded Reference Phantoms

Figure 3.8 plots the gamma index analysis results for the comparison of the printed and molded anthropomorphic slabs for all ROIs (see Figure 2.11). The gamma index analysis pass rates were generally higher at 12, 16, and 20 MeV than at 6 and 9 MeV electron energies. At all energies considered, the pass rates were highest in ROI 3, intermediate in ROI 1, and lowest in ROI 2. The mean gamma index and its standard deviation for the 6 MeV measurements across

all ROIs indicate very poor dosimetric agreement. This was expected due to 6 MeV electrons having an R_{50} of 3 cm in water and the printed slab having a thickness of 2.92 cm WET (Table 3.9).

Table 3.9. The 50% ionization depth, R_{50} and calculated WET for the printed anthropomorphic slab. The R_{50} and t_w are both listed as depth in water.

Electron Beam Energy (MeV)	R_{50} (cm)	t_w (cm WET)
6	2.38	2.92
9	3.26	2.92
12	4.80	2.92
16	6.30	2.92
20	7.89	2.92

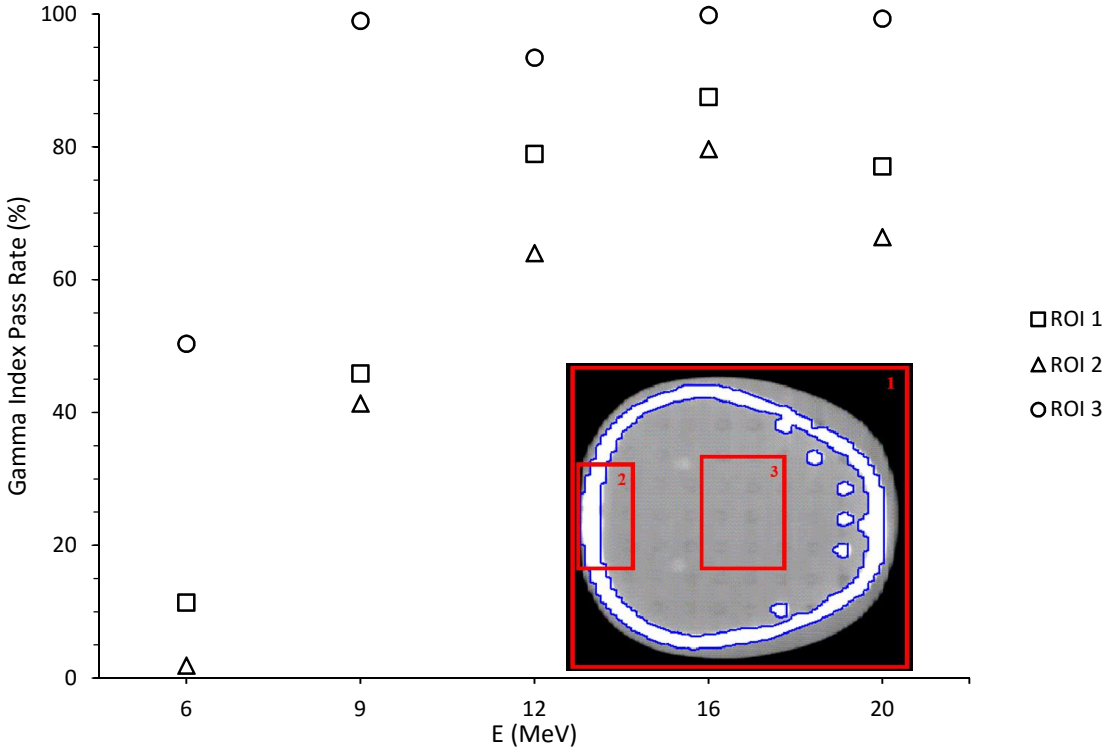

Figure 3.8. Gamma index analysis pass rates for the dosimetric comparison of the molded and printed anthropomorphic slabs. ROIs 1 (squares), 2 (triangles), and 3 (circles) refer to the different regions of interest indicated in Figure 2.11.

Table 3.10 lists the gamma index pass rates for ROI 1. A representative gamma index map for 12 MeV electrons is shown in Figure 3.9. In this graphic the red regions, which indicate a gamma index value greater than 1 (fail), are largely the result of lateral disequilibrium caused by heterogeneities in the molded slab. The greyscale regions have a gamma index value less than 1 (pass). Given the limited interval of mass densities that could be printed in this study, these bone heterogeneities were not replicated in the printed slab. The interior region shows that for a homogeneous soft tissue, the printed slab has good dosimetric agreement with the molded reference slab. Figures 3.10 and 3.11 show a comparison of the two slabs. The bone heterogeneities within the molded slab are contoured to facilitate visual correlation of their location relative to the gamma index failing regions.

Table 3.10. The mean, standard deviation, and pass rate for the gamma index analyses of ROI 1. The mean and standard deviation values for each energy are indicators of the dosimetric agreement between the two slabs.

Electron Beam Energy (MeV)	Gamma Index		Pass Rate (%)
	$\bar{\Gamma}_{(r_m, r_c)}$	$\sigma_{\bar{\Gamma}}$	
6	33.7	41.4	11.4
9	1.8	1.7	45.9
12	0.6	0.6	78.9
16	0.5	0.5	87.5
20	0.7	0.6	77.1

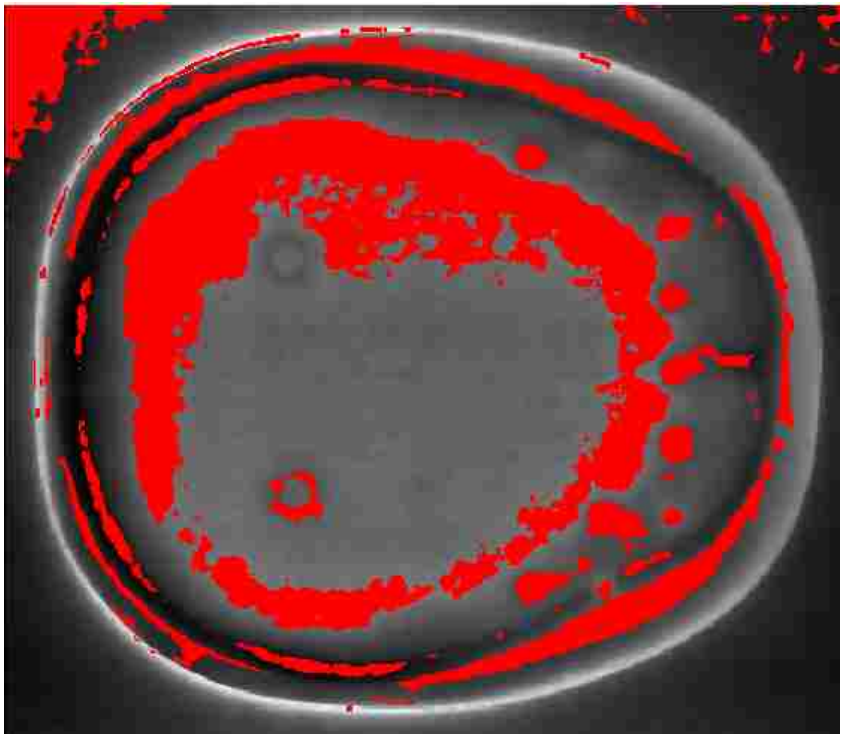

Figure 3.9. Graphic of the full image gamma index map for the printed and molded anthropomorphic slab irradiations. The irradiations were performed using a therapeutic 12 MeV electron beam. The red regions are failing points and the greyscale regions are passing points.

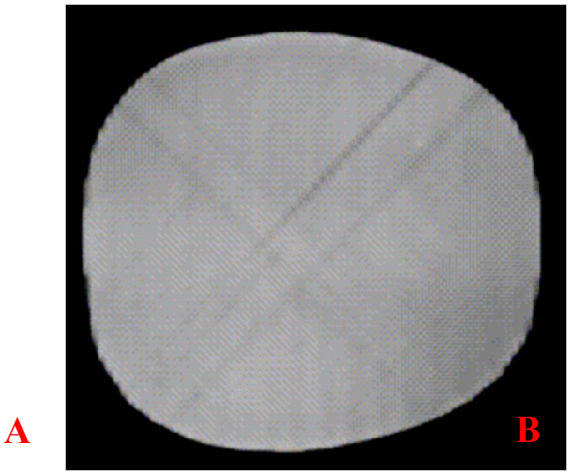

Figure 3.10. Comparison of axial CT images of the molded and printed anthropomorphic slabs. The bone heterogeneities in the molded slab (A) are contoured in blue. The printed slab (B) doesn't feature any of these heterogeneities by design (see Section 2.2.1), and shows printing

structures. The large ring is the cranial bone, and the circular points are bone tissue substitute plugs that are part of the reference phantom design for dosimetry applications.

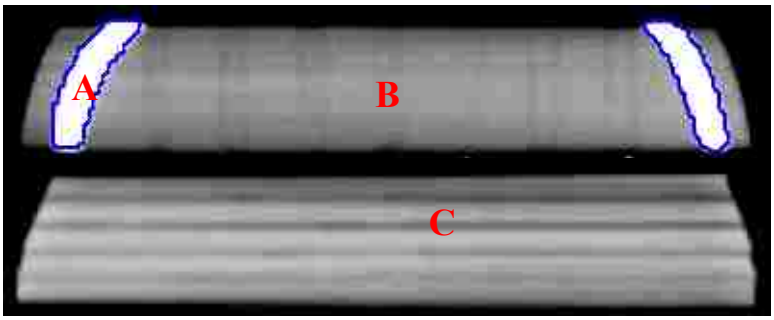

Figure 3.11. Comparison of sagittal CT images of the molded (top) and printed (bottom) slabs. The bone heterogeneity in the molded slab is contoured in blue. The printed slab doesn't feature these heterogeneities by design. Item (A) indicates the molded slab bone heterogeneity, (B) homogeneous brain tissue, and (C) the air gaps separating the ROIs in the printed slab design, respectively.

Table 3.11 lists the gamma index analysis results for ROI 2. This ROI examined the effect of a bone/soft tissue interface on the gamma index analysis comparing the printed and molded slabs. The pass rate increases significantly with electron energy due to the decreasing influence of multiple coulomb scatter. Figure 3.12 plots gamma index maps of ROI 2 for multiple electron energies.

Table 3.11. The mean, standard deviation, and pass rate percentages for the gamma index analyses of ROI 2 (Figure 2.11). The mean and standard deviation values for each energy are indicators of the dosimetric agreement between the two slabs.

Electron Beam Energy (MeV)	Gamma Index		Pass Rate (%)
	$\bar{\Gamma}_{(r_m,r_c)}$	$\sigma_{\bar{\Gamma}}$	
6	13.4	8.5	1.9
9	2.4	2.5	41.3
12	1.0	0.8	64.0
16	0.7	0.4	79.7
20	0.9	0.7	66.4

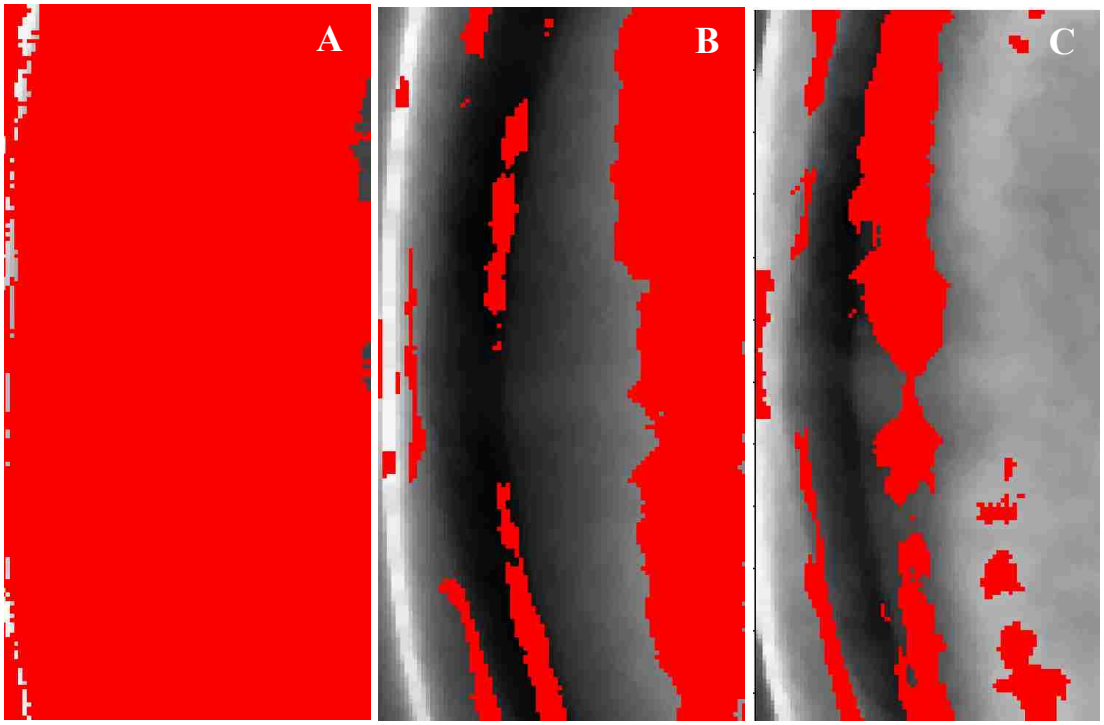

Figure 3.12. ROI 2 gamma index maps for 6, 12, and 20 MeV electron irradiations. The red regions indicate points with a gamma index of greater than 1 (fail), and the grey regions are points with a gamma index of less than 1 (pass). The number of failing points is shown to decrease with increasing electron energy, from 6 (A) to 12 (B) to 20 (C) MeV.

The gamma analysis results for ROI 3 are listed in Table 3.12. This ROI examined a large homogeneous region to compare the printed and molded slabs (Figure 2.11). The pass rates for all energies except 6 MeV show clinically acceptable agreement between the printed and molded slabs. The failures for the 6 MeV analysis are due to the ranging out of electrons through the slabs as mentioned above. Figure 3.13 plots an example gamma index map of the brain ROI for 12 MeV electrons.

Table 3.12. The mean, standard deviation, and pass rate percentages for the gamma index analyses of ROI 3 (Figure 2.11). The mean and standard deviation values for each energy are indicators of the dosimetric agreement between the two slabs.

Electron Beam Energy (MeV)	Gamma Index		Pass Rate (%)
	$\bar{\Gamma}_{(r_m,r_c)}$	$\sigma_{\bar{\Gamma}}$	
6	1.3	1.0	50.4
9	0.3	0.2	99.0
12	0.4	0.3	93.5
16	0.2	0.12	99.8
20	0.3	0.2	99.3

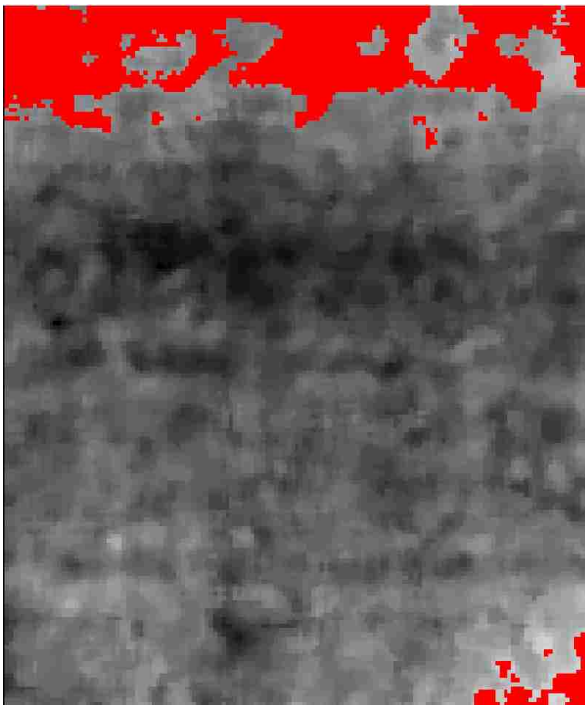

Figure 3.13. A gamma index map for ROI 3 for 12 MeV electrons. The red regions indicate points with a gamma index of greater than 1 (fail), and the grey regions are points with a gamma index of less than 1 (pass). The number of failing points along the ROI edges are a result of lateral disequilibrium from the bone heterogeneity.

Overall the printed slab showed acceptable dosimetric agreement with the molded slab. For 12, 16, and 20 MeV electron energies the gamma index pass rates surpassed the 60% value stated in the hypothesis for all three ROIs, and surpassed the clinical standard of 90% for ROI 3. The gamma index failures are largely the result of not being able to print bone. The lack of bone heterogeneities also affected the lateral scattering of 9 MeV electrons, a reason for the lower pass rates for this energy trial. The 6 MeV irradiations were affected by measuring near the end of particle range in the slabs for this aim.

3.3. Aim 3: Comparison of Printed Personalized Phantom to Molded Reference Phantom

The comparison of dose calculations for the personalized head phantom and reference head phantom to dose calculations in the patient served as an integral test of the hypothesis of this work. In this aim we printed a head phantom from patient imaging data, then performed electron beam dose calculations on the patient, printed phantom, and reference phantom (see Section 2.3.3). The calculated doses for both the printed and reference phantom were then compared with the calculated dose for the patient using gamma index analysis to assess how well each phantom models radiologic characteristics of the patient.

Table 3.13 lists the gamma index pass rates for the comparisons of both the printed head phantom to the patient and the reference phantom head to the patient. For gamma index criteria of 3% DD or 3 mm DTA, only 16 and 20 MeV energy trials for the comparison of the printed phantom to the patient exceeded a pass rate of 60%. For all energy trials, the personalized phantom showed substantial improvement in gamma index pass rates over the reference phantom head. This is due to the personalized phantom more accurately modeling the patient surface anatomy and low density heterogeneities than the reference phantom. Figure 3.14 shows dose

distributions of the electron beam dose calculations for the patient and both the personalized and reference phantoms for a therapeutic 6 MeV electron beam.

The differences in dose distributions in the printed personalized phantom and the patient were largely a result of the inability to print bone for this study, but this was accounted for with overriding the tissue densities in the patient to facilitate a more direct comparison (Section 2.3.2). Despite only being able to produce phantoms with one tissue density, the printed personalized phantom still showed marked improvement over the reference phantom due to its ability to more accurately model surface geometry and the low density heterogeneities such as tissue-sinus interfaces present in craniofacial anatomy.

Table 3.13. The gamma index analysis pass rates for the dosimetric comparison of both the personalized and anthropomorphic head phantoms to the patient at 6 to 20 MeV electron beam energies.

Electron Beam Energy (MeV)	Gamma Index Pass Rate (%)	
	Personalized Printed Phantom	Reference Molded Phantom
6	40.7	27.3
9	43.7	25.8
12	53.4	28.1
16	63.3	32.8
20	69.7	41.3

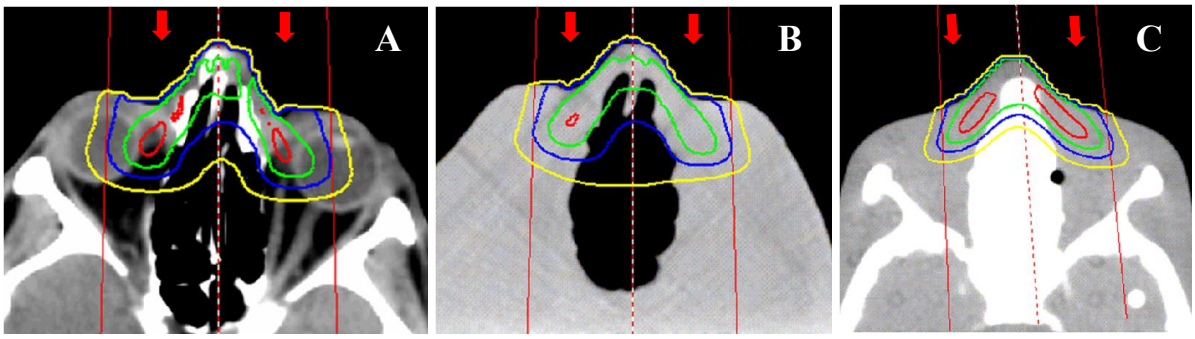

Figure 3.14. Transverse treatment planning images of the 6 MeV calculated dose distributions in (A) the patient, (B) the printed phantom, and (C) the reference phantom. The red, blue, green, and yellow isodose lines correspond to 80, 60, 40, and 20% of the maximum dose. The beam placement is shown by the red lines and the beam direction is indicated by the red arrows.

The dose distributions in Figure 3.14 show that, while the surface anatomy of the printed phantom provides isodose distributions with a similar shape to those in the patient, the electron ranges differ in distal regions. This is further revealed in the gamma index maps shown in Figure 3.15. The large majority of the failing points in gamma analysis are due to a deeper distal dose falloff in the printed phantom compared to the patient.

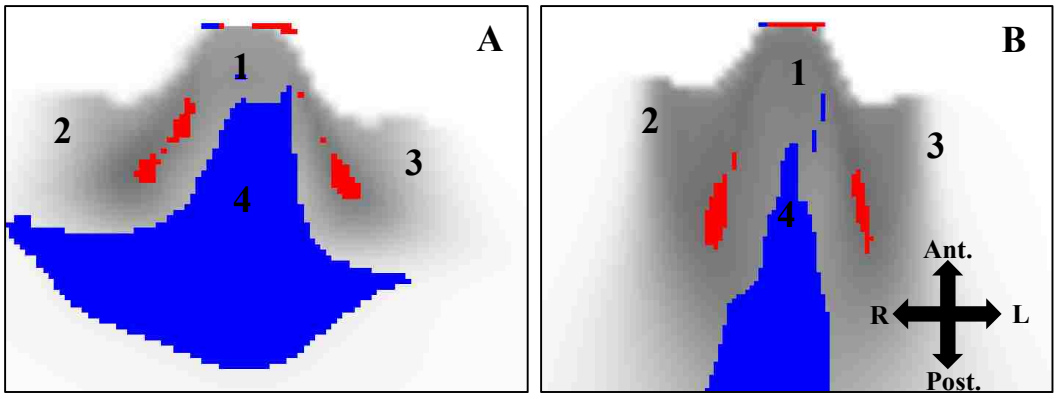

Figure 3.15. Axial gamma index maps comparing the printed phantom to the patient for 6 and 20 MeV electron beams. The 6 MeV gamma map (A) shows greater lateral disequilibrium compared to the 20 MeV gamma map (B). The red regions represent failing points where the patient exhibited a higher dose, and the blue regions represent failing points where the phantom exhibited a higher dose. The beam direction is anterior to posterior, and the patient anatomy is indicated by (1) the nose, (2) right cheek, (3) left cheek, and (4) the ethmoidal sinus.

To further examine the dose differences between the patient and the printed phantom, additional gamma analyses were performed for the personalized phantom with looser gamma index criteria of 5% DD or 3 mm DTA and 3% DD or 5 mm DTA. The results for these analyses are listed in Table 3.14. The looser DTA criteria reflected the previous findings (Section 3.2) on the differences in attenuation properties between printed materials and reference materials designed to represent human tissue. This is seen in the increased pass rates for 5 mm DTA compared to a DTA of 3 mm (Table 3.14), adding confidence to the pass rates shown in Table 3.12 because it shows that the gamma index results vary smoothly with different DTA and DD. This indicates that the findings were not strongly influence by the particular choice of DD in the gamma index criteria.

Table 3.14. The gamma index analysis pass rates for the dosimetric comparison of the personalized head phantom to the patient for electron beam dose calculations. Pass rates are listed for criteria combinations of 3% and 5% DD and 3 and 5 mm DTA.

Energy (MeV)	Gamma Index Pass Rate (%)		
	3%, 3 mm	5%, 3 mm	3%, 5 mm
6	40.7	41.5	50.4
9	43.7	44.8	53.4
12	53.4	55.6	65.4
16	63.3	66.2	75.3
20	69.7	72.9	78.6

The printed phantom showed substantially better dosimetric accuracy than the reference phantom for modeling the patient dose calculations (Section 2.3.2). The primary reason for the dosimetric differences in the printed phantom and the patient is the inability to print bone. The lack of bone heterogeneities prevents the energy attenuation and lateral scattering that is caused by this heterogeneity in the patient. Other sources of dosimetric differences are the ranging out of electrons in regions with large mass thickness differences between the phantom and the patient, and the lateral scattering of electrons at 6 and 9 MeV electron energies.

Chapter 4: Discussion

This work tested the hypothesis that personalized printed phantoms can achieve a pass rate of greater than 60% for electron beam radiotherapy treatments with clinically relevant gamma index criteria. The hypothesis was proven true for higher electron energies of 16 and 20 MeV and disproven at electron energies of 6, 9, and 12 MeV. This was accomplished by using electron beam measurements and calculations for a variety of materials and geometries to determine the radiological properties of reference phantoms and 3D printed personalized phantoms. The print materials, fabrication techniques, and geometric accuracy of 3D printing were studied as a means of testing whether or not 3D printed phantoms designed from patient imaging data could serve as an improvement over reference anthropomorphic phantoms for radiation dose measurements in clinical research and radiotherapy applications.

The tests of the print materials and fabrication techniques revealed that the printing process introduces minute voids into solid printed objects, which affected the mass density and attenuation properties of printed materials. In measuring the radiation attenuation properties of printed slabs, we showed that it is possible to mimic both the radiological and physical thickness of tissue with a density less than 1.14 g/cm^3. We could not accomplish this for higher density tissue given the printer limitations in filament density. The differences between the calculated and measured WET for the printed slabs can be attributed to the deviations in printed slab mass thickness from the design parameters.

Aim 2, the comparison of printed and molded reference anthropomorphic slabs, showed that a 3D printed slab has the potential to achieve radiological equivalency with a molded reference slab. Further improvements in radiological equivalency between the printed and molded slab could be made by modeling bone in the printed slab. The PLA proved to be a

suitable material for soft tissue, as shown by the gamma index pass rates for ROI 2. These findings are reinforced by the gamma index analysis results from Aim 3, the comparison of the personalized printed phantom to the patient for electron beam dose calculations. Additionally, we showed that for a patient with atypical anatomy, personalized printed phantoms can achieve higher dosimetric accuracy than a generic molded phantom when compared with the patient.

4.1. Impact

Personalized 3D printed phantoms have the potential to be utilized as a quality assurance tool in radiotherapy to facilitate measuring dose from patient radiotherapy plans. This tool could be useful in assessing the accuracy of radiotherapy plans for patients with gross anatomical deficiencies in comparison to reference anatomy. Treatment planning systems may not accurately predict dose distributions for radiotherapy cases in which there are in-field heterogeneities, such as the bony processes previously discussed in Section 1.1.3 and post-operative abnormalities. Personalized phantoms could be used as a tool to perform radiation dose measurements of a personalized radiotherapy plan in the presence of heterogeneities. Partial amputations or scars can significantly affect surface geometry, which confirms the findings of this study that have shown to have a sizable impact on electron beam dose distributions (Hogstrom, Mills, and Almond 1981). For cases such as these, 3D printed personalized phantoms have proven capable of providing a more accurate dosimetric assessment of the effects of heterogeneities on dose distributions both at the surface of and within the patient.

The findings of this study can also find applicability in the improvement of dose calculation algorithms in radiotherapy treatment planning. Specifically, 3D printed patient-specific phantoms with atypical anatomy could be utilized to perform dose measurements for radiotherapy treatment plans in order to validate planned dose calculations in the presence of

gross anatomical heterogeneities. This would potentially provide enhanced dose coverage and tissue sparing in patient radiotherapy plans, thereby improving patient outcomes. Another clinical use for the findings of this study would be print personalized phantoms that can accommodate prostheses or implants (Figure 4.1). Extensive Monte Carlo studies have been done on the dosimetric impact of implants such as surgical screws or radiotherapy fiducial markers (Vassiliev et al. 2012, Wang et al. 2013). Additionally, the effects of fiducial markers on dose distributions has been quantified with dosimetric measurements in anthropomorphic phantoms (Huang et al. 2011, Newhauser et al. 2007). Performing dosimetric measurements using personalized phantoms for these studies could provide potentially enhanced dosimetric accuracy and improved understanding of the impact of these implanted heterogeneities. Another possible application would be to be able to print geometrically accurate phantoms of the fetus during different gestational stages, which would allow for better fetal dose measurements from out of field doses.

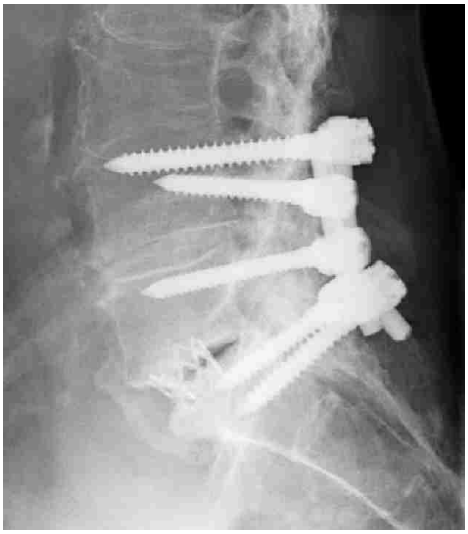

Figure 4.1. Radiograph of surgical pins used to bridge lumbar and sacral vertebrae following after a spinal fusion to treat spinal stenosis. These high density surgical implants can cause significant dose perturbations for radiotherapy treatments (rad.washington.edu).

4.2. Previous Literature

Similar to the previous study of personalized phantoms by Ehler et al. (2014), we found that 3D printing is a feasible tool for fabricating personalized phantoms for electron beam radiotherapy. Regarding the use of fused deposition modeling as the chosen printing technology, a study on 3D printed plastics for use in proton therapy found that this printing technology is inferior in comparison to Polyjet printing for charged particle therapy applications (Lindsay et al. 2015). They found similar visual printing errors (see Figure 2.13) and density variations due to voids introduced by the printing process. A study of 3d printed bolus for charged particle therapies, Zou et al. (2015) showed that printed electron bolus created with PLA caused a submillimeter depth shift in the 90% isodose line for therapeutic electron beams. The findings are similar in nature to those of the first aim in regard to deviations in range shifts compared with predicted values. While these findings are significant and warrant further investigation into fused deposition modeling as a printing technology, the deviations in range shifts are still within a clinically acceptable range of 2 mm for the lung slab and 4 mm for the bone slab.

4.3. Study Strengths

To the best of our knowledge, this is the first study to examine the feasibility of 3D printed phantoms that model both internal and external patient geometry for electron beam therapy. For each aim we sampled all clinically relevant electron energies and examined changes in dose distributions for different electron energies. Additionally, this study encompassed a wide range of mass densities in both printed and reference geometries in regards to their physical properties and radiological attenuation properties for therapeutic electron beams.

4.4. Study Limitations

Limitations of this study are primarily the result of the technology available for 3D printed phantom production. Due to limitations in printing technology available to us for this study, we were not able to test personalized phantoms with patient-specific bone heterogeneities so we could not assess the dosimetric impact they would have. Given the performance of the personalized phantom in comparison to the reference phantom, this is considered to be a minor problem. Further developments in printer materials and upgraded printing technology could overcome this issue.

For the first aim, we were unable to verify the mass densities for the lung and bone reference slabs in comparison to the densities stated by the manufacturers. Given that the radiological thickness of these reference slabs was measured using range shift techniques, this was not a serious limitation to this aim. The layering process utilized in fused deposition printing introduces density variations in printed structures, which were determined to introduce attenuation variability and scattering in objects printed with 100% infill density. Also, the full effect of how various infill patterns and infill densities influence the object mass density and the degradation of electron beam range is not fully understood. These factors have the potential to introduce an angular dependence to printed phantoms. While these limitations warrant further investigation, they can be considered to be minor issues in phantom fabrication. Fused deposition printing with multiple filaments would allow for a broader range of printable plastic densities. The ability to print with a plastic that is of similar density to bone in addition to a soft tissue equivalent plastic would permit modeling high density heterogeneities such as bone. From the results of the second and third aims of this work, it can be concluded that this improvement would significantly improve printed phantom accuracy.

The stacking of layers limits the ability to prototype features that have no underneath supporting structure. The use of a different 3D printing modality, such as the stereolithography process shown in Figure 4.2, would compensate some of these limitations because of different fabrication techniques (Wong and Hernandez 2012).

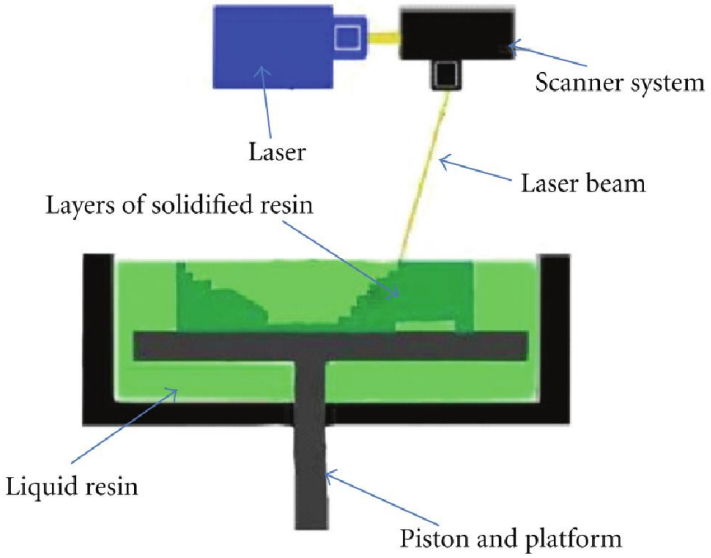

Figure 4.2. Graphic of the stereolithography 3D printing process. This method uses a scanned laser to solidify the surface layer in a liquid resin bath. The print platform is adjusted as the structure is prototyped to build the height of the printed structure. This process allows for a continuous solid printed object, an advantage over the fused deposition layering process. Image adapted from Wong and Hernandez (2012).

Another limitation of this study is the phantom design process. More detailed imaging data would permit higher resolution in the conversion of imaging data to structural design. Decreasing CT slice thickness would improve the geometric data available, but at a cost of increased patient dose. Other imaging modalities such as MRI warrant investigation as well. The current method of using treatment planning tools for structure delineation also can introduce errors in structure design. By implementing a better method of identifying density gradients, more accurate contours could be drawn to improve the phantom geometric accuracy. This study

utilized the TPS and an in-house stitching program to produce the phantom design, which limited the resolution of the surface mesh. Continued refinement of the stitching program would also increase surface resolution. Alternatively, integrating image analysis software into the design process could provide improvements in STL file production.

4.5. Future Work

The findings of this work lay the framework for several future studies utilizing personalized 3D printed phantoms. The findings of this study could also find applicability in different aspects of radiation oncology, including improved anthropomorphic dosimetry and radiobiological studies.

4.5.1. Validation for Other Therapy Modalities

Given the differences in radiation transport and dose deposition for different types of radiation therapy, it is important to repeat this study for other external beam therapy modalities. Repeating the methods described in Section 2.3.2 for x-ray treatments would prove the utility of printed phantoms for another commonly used radiotherapy modality. Doing the same for proton therapy treatments would provide confirmation as to whether or not personalized phantoms are suitable for measuring absorbed doses to deep-seated targets. An assessment of the potential angular dependence of printed phantoms should be included in any future charged particle therapy studies.

4.5.2. Validation for Other Anatomical Regions

To the best of our knowledge, printed personalized phantoms have not been extensively studied for any anatomical region other than the head. Similar to features of the head, the female breast can vary drastically from person to person in terms of density, size, and shape. The development of patient-specific breast phantoms may allow for improvements in dosimetry of

radiotherapy treatments for breast cancer, as the geometry of the breast can be more accurately modeled to reflect the patient anatomy under treatment conditions. Alternatively, the phantom design techniques described in Section 2.3.1 could be adapted to produce patient-specific breast immobilization devices akin to the head immobilization devices tested by Fisher et al. (2014).

4.5.3. In-House Phantom Manufacturing

This study looked at the potential for producing 3D printed phantoms in-house, an advantage for clinical applications that require rapid fabrication. 3D printing hardware is the only technology used in this work that is not readily available in most radiation oncology clinics across the U.S. A dual filament extrusion deposition 3D printed would cost around $5000, while 100 kg of PLA filament costs approximately $3000. All of the necessary software for designing and producing personalized phantoms is either freely available or already integrated into clinical software e.g. a radiotherapy TPS. A radiation oncology center could acquire all the necessary tools to produce personalized phantoms at approximately a fifth of the cost of an adult male reference phantom. So for a fraction of the cost of currently available anthropomorphic phantoms, clinics could design and print phantoms in-house. This would also allow for printed phantoms to be modified during design to utilize the dosimetry tools currently available to a clinic. For example, personalized phantoms could be prototyped to support various types of ion chambers, thermoluminescent dosimeters, or film. Additionally, dosimeters could be printed with geometry tailored to specific applications e.g. measuring doses in a personalized phantom sinus cavity.

4.5.4. Future Applications

One potential future application for these findings is the development of more advanced radiotherapy phantoms. Current phantoms have the limitation of being rigid structures with

limited dosimetric capabilities, variations in density for replicated tissue, and anatomical detail resolution. These limitations could be overcome by the development of hybrid phantoms: printed phantoms that can be combined with other materials to fulfill a new role in dose measurements.

The simplest hybrid phantom design involves adding voids in the design process that could be filled with tissue equivalent materials or gel dosimeters. The phantom design methods would be similar to those described in Section 2.3.1, but with the additional delineation of the voids to be filled. For example, a phantom could be designed and printed with the ability to fill in bone heterogeneities. During phantom processing, the bone contours would be rendered as voids in the phantom design structure. After printing, the voids would be filled with a pourable material with a tissue equivalency similar to that of bone and allowed to set. The resulting phantom would be able to mimic soft tissue, as verified by the results in Section 3.2.3, as well as bone and sinus cavities. Alternatively, a hollow patient-specific phantom could be printed that would accommodate gel dosimeters such as BANG® polymer gel. The gel dosimeter fill would provide three-dimensional internal dose information for radiotherapy treatments, while the 3D printed exterior would accurately model patient surface anatomy.

Another application is the use of the phantom design process to create molds for anatomically accurate dosimeters. A recent study examining the accuracy of microSBRT treatments with the use of 3D printed rodent-morphic dosimeters utilized phantoms created from 3D printed molds (Bache et al. 2015). The dosimeters in this work consisted of an abdominal section and high-Z insert, both cast using 3D molds designed from rodent imaging data (Figure 4.3). This technique could be adapted to develop anatomically correct dosimeters for patient radiotherapy treatments. Potential anatomical regions for which these hybrid phantoms could improve dose measurements are head and breast phantoms.

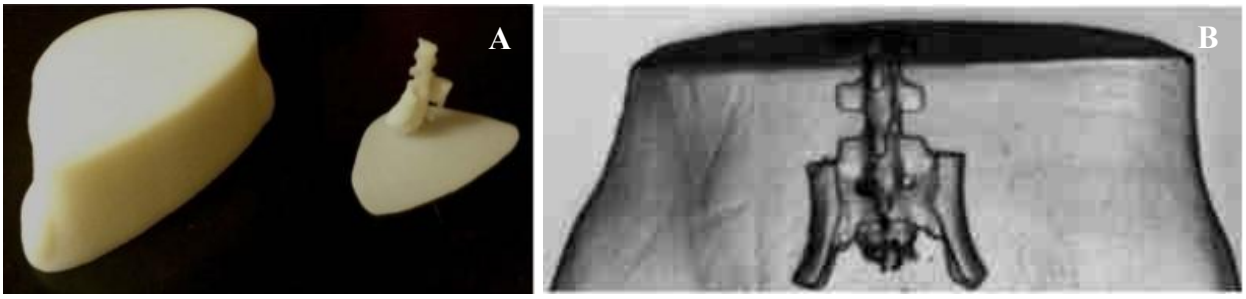

Figure 4.3. 3D printed molds and an optical CT projection of a gel dosimeter with high-Z insert. The molds (A) were designed from imaging data, and the CT projection (B) shows the full phantom. This hybrid phantom serves as a rodent-morphic dosimeter with a high-Z insert, serving as a realistic representation of rodent anatomy. Image adapted from Bache et al., (2015).

Hybrid phantoms composed of both printed thermoplastics and printed biological material such as cell scaffolding or tissue would take advantage of the rapid advances in 3D printing technologies for the creation of biological material. Cell scaffolding or skin tissue could be printed directly onto personalized phantoms and then utilized in dose measurements, providing radiobiological feedback. These radiobiological hybrid phantoms could provide valuable biological data for assessments of deterministic effects associated with radiation exposure. A clinically significant application for this technology would be in quantifying biological endpoints for normal tissue complication risk models.

This idea is supported by studies such as the recent work by Marchioli et al. (2015) , which studies the use of 3D printed scaffolds for Islets of Langerhans transplants in the treatment of Type I Diabetes. This work used 3D bioplotting to fabricate porous scaffolds that would allow for vascularization of the transplant site, which would provide improved nutrient flow and oxygenation. With continued improvements in biological material and cell culture technology, the techniques and findings of this study could be applied to personalized radiotherapy phantoms to develop hybrid phantoms for tumor response studies. Patient-specific printed phantoms could

have tumors printed into them for dose measurements to assess the impact of radiotherapy treatments, with the benefit of cell survival studies in a three dimensional geometry.

Chapter 5: Conclusion

This study demonstrated that while personalized printed phantoms can achieve a gamma analysis pass rate of greater than 60% at 16 and 20 MeV electron beam energies, further improvements to printed phantoms are necessary in order to meet this goal at lower therapeutic electron beam energies. Additionally, it was shown that personalized printed phantoms are capable of achieving significant improvements in dosimetric accuracy for electron therapy plans over molded reference anthropomorphic phantoms when compared with patient dose calculations, i.e. for a case where the patient anatomy and reference anatomy differ substantially. The findings of this study suggest that better dosimetric results could be achieved with a wider range of densities for printed materials.

While the findings of this study are promising, significant improvements in printed phantoms are necessary to achieve clinically acceptable gamma analysis pass rates, e.g., 90% with a criteria of 3% DD or 3 mm DTA. Several of these improvements can be made with improved printing technology and refinement of the software used in the phantom design process. Additional developments in phantom design software, fabrication materials, and 3D printing technologies will improve the utility of personalized phantoms in both a clinical and academic environment.

References

Almond, P. R., P. J. Biggs, B. M. Coursey, W. F. Hanson, M. S. Huq, R. Nath, and D. W. Rogers. 1999. "AAPM's TG-51 protocol for clinical reference dosimetry of high-energy photon and electron beams." *Med Phys* 26 (9):1847-70.

ASTM. 2009. D4142-89: Standard Guide for Testing Epoxy Resins. West Conshohocken, PA: ASTM International.

Avelino, S. R., L. F. O. Silva, and C. J. Miosso. 2012. "Use of 3D-Printers to Create Intensity-Modulated Radiotherapy Compensator Blocks." 34th Annual International Conference of the IEEE EMBS, San Diego, California USA.

Bache, S. T., T. Juang, M. D. Belley, B. F. Koontz, J. Adamovics, T. T. Yoshizumi, D. G. Kirsch, and M. Oldham. 2015. "Investigating the accuracy of microstereotactic-body-radiotherapy utilizing anatomically accurate 3D printed rodent-morphic dosimeters." *Med Phys* 42 (2):846-55.

Bert, C., and M. Durante. 2011. "Motion in radiotherapy: particle therapy." *Phys Med Biol* 56 (16):R113-44.

DeWerd, L. A., and M. Kissick. 2014. *The Phantoms of Medical and Health Physics*: Springer.

Ehler, E. D., B. M. Barney, P. D. Higgins, and K. E. Dusenbery. 2014. "Patient specific 3D printed phantom for IMRT quality assurance." *Phys Med Biol* 59 (19):5763-73.

Eley, J. G., W. D. Newhauser, R. Luchtenborg, C. Graeff, and C. Bert. 2014. "4D optimization of scanned ion beam tracking therapy for moving tumors." *Phys Med Biol* 59 (13):3431-52.

Fisher, M., C. Applegate, M. Ryalat, S. Laycock, M. Hulse, D. Emmens, and D. Bell. 2014. "Evaluation of 3-D Printed Immobilisation Shells for Head and Neck IMRT." *Open Journal of Radiology* 04 (04):322-328.

Hogstrom, K. R., and P. R. Almond. 2006. "Review of electron beam therapy physics." *Phys Med Biol* 51 (13):R455-89.

Hogstrom, K. R., M. D. Mills, and P. R. Almond. 1981. "Electron beam dose calculations." *Phys Med Biol* 26 (3):445-59.

Huang, J. Y., W. D. Newhauser, X. R. Zhu, A. K. Lee, and R. J. Kudchadker. 2011. "Investigation of dose perturbations and the radiographic visibility of potential fiducials for proton radiation therapy of the prostate." *Phys Med Biol* 56 (16):5287-302.

ICRU. 1984a. Electron beams with energies between 1 and 50 MeV. In *ICRU Report 35*. International Commission on Radiation Units and Measurements.

ICRU. 1984b. Stopping Powers for Electrons and Positrons. In *ICRU Report 37*: International Commission on Radiation Units and Measurements.

Ju, S. G., M. K. Kim, C. S. Hong, J. S. Kim, Y. Han, D. H. Choi, D. Shin, and S. B. Lee. 2014. "New technique for developing a proton range compensator with use of a 3-dimensional printer." *Int J Radiat Oncol Biol Phys* 88 (2):453-8.

Khan, F. M., K. P. Doppke, K. R. Hogstrom, G. J. Kutcher, R. Nath, S. C. Prasad, J. A. Purdy, M. Rozenfeld, and B. L. Werner. 1991. "Clinical electron-beam dosimetry: Report of AAPM Radiation Therapy Committee Task Group No. 25." *Med Phys* 18 (1):73-109.

Lee, C., D. Lodwick, D. Hasenauer, J. L. Williams, C. Lee, and W. E. Bolch. 2007. "Hybrid computational phantoms of the male and female newborn patient: NURBS-based whole-body models." *Phys Med Biol* 52 (12):3309-33.

Lindsay, C., J. Kumlin, A. Jirasek, R. Lee, D. M. Martinez, P. Schaffer, and C. Hoehr. 2015. "3D printed plastics for beam modulation in proton therapy." *Phys Med Biol* 60 (11):N231-40.

Low, D. A., W. B. Harms, S. Mutic, and J. A. Purdy. 1998. "A technique for the quantitative evaluation of dose distributions." *Med Phys* 25 (5):656-61.

Marchioli, G., L. van Gurp, P. P. van Krieken, D. Stamatialis, M. Engelse, C. A. van Blitterswijk, M. B. Karperien, E. de Koning, J. Alblas, L. Moroni, and A. A. van Apeldoorn. 2015. "Fabrication of three-dimensional bioplotted hydrogel scaffolds for islets of Langerhans transplantation." *Biofabrication* 7 (2):025009.

McKenzie, E. M., P. A. Balter, F. C. Stingo, J. Jones, D. S. Followill, and S. F. Kry. 2014. "Toward optimizing patient-specific IMRT QA techniques in the accurate detection of dosimetrically acceptable and unacceptable patient plans." *Med Phys* 41 (12):121702.

Menzel, H. G., C. Clement, and P. DeLuca. 2008. "ICRP Publication 110. Realistic reference phantoms: an ICRP/ICRU joint effort. A report of adult reference computational phantoms." *Annals of the ICRP* 39 (2):1-164.

Newhauser, W. D., J. D. Fontenot, A. Mahajan, D. Kornguth, M. Stovall, Y. Zheng, P. J. Taddei, D. Mirkovic, R. Mohan, J. D. Cox, and S. Woo. 2009. "The risk of developing a second cancer after receiving craniospinal proton irradiation." *Phys Med Biol* 54 (8):2277-91.

Newhauser, W. D., N. C. Koch, J. D. Fontenot, S. J. Rosenthal, D. S. Gombos, M. M. Fitzek, and R. Mohan. 2007. "Dosimetric impact of tantalum markers used in the treatment of uveal melanoma with proton beam therapy." *Phys Med Biol* 52 (13):3979-3990.

Niroomand-Rad, A., C. R. Blackwell, B. M. Coursey, K. P. Gall, J. M. Galvin, W. L. McLaughlin, A. S. Meigooni, R. Nath, J. E. Rodgers, and C. G. Soares. 1998. "Radiochromic film dosimetry: recommendations of AAPM Radiation Therapy Committee Task Group 55. American Association of Physicists in Medicine." *Med Phys* 25 (11):2093-115.

Paelinck, L., W. De Neve, and C. DeWagter. 2007. "Precautions and strategies in using a commercial flatbed scanner for radiochromic film dosimetry." *Physics in Medicine and Biology* 52 (1):231-242.

Rengier, F., A. Mehndiratta, H. von Tengg-Kobligk, C. M. Zechmann, R. Unterhinninghofen, H. U. Kauczor, and F. L. Giesel. 2010. "3D printing based on imaging data: review of medical applications." *Int J Comput Assist Radiol Surg* 5 (4):335-41.

Smart, D. R. 2000. *Physician Characteristics and Distribution in the US*: American Medical Association Press.

Snyder, W. S., M. Cook, E. Nasset, L. Karhausen, G. P. Howells, and I. Tipton. 1975. ICRP Publication 23: report of the task group on reference man. International Commission on Radiation Protection.

Taylor, J. R. 1982. *An Introduction to Error Analysis: The Study of Uncertainties in Physical Measurements*. Mill Valley, CA: Univ. Sci. Books.

Valentin, J. 2002. Basic anatomical and physiological data for use in radiological protection: reference values: ICRP Publication 89. In *Annals of the ICRP*: International Commission on Radiation Protection.

Vassiliev, O. N., R. J. Kudchadker, D. A. Kuban, S. J. Frank, S. Choi, Q. Nguyen, and A. K. Lee. 2012. "Dosimetric impact of fiducial markers in patients undergoing photon beam radiation therapy." *Phys Med* 28 (3):240-4.

Wang, X., J. N. Yang, X. Li, R. Tailor, O. Vassilliev, P. Brown, L. Rhines, and E. Chang. 2013. "Effect of spine hardware on small spinal stereotactic radiosurgery dosimetry." *Phys Med Biol* 58 (19):6733-47.

Wong, K. V., and A. Hernandez. 2012. "A Review of Additive Manufacturing." *ISRN Mechanical Engineering* 2012:1-10.

Zhang, R., and W. D. Newhauser. 2009. "Calculation of water equivalent thickness of materials of arbitrary density, elemental composition and thickness in proton beam irradiation." *Phys Med Biol* 54 (6):1383-95.

Zou, W., T. Fisher, M. Zhang, L. Kim, T. Chen, V. Narra, B. Swann, R. Singh, R. Siderit, L. Yin, B. K. Teo, M. McKenna, J. McDonough, and Y. J. Ning. 2015. "Potential of 3D printing technologies for fabrication of electron bolus and proton compensators." *J Appl Clin Med Phys* 16 (3):4959.

Vita

Andrew Halloran was born in Austin, Texas to Sharon and Michael Halloran. After graduating from Lake Travis High School in 2007, he chose to move to Baton Rouge to attend Louisiana State University and major in engineering. Andrew quickly realized that engineering was not his cup of tea and realigned his academic pursuits to major in physics with a concentration in medical and health physics. Upon graduating in December of 2011, Andrew took a position as an intern under the radiation safety officer at Mary Bird Perkins Cancer Center in Baton Rouge. In June of 2012 he married Priscilla Terrase, as the two concluded that the life of a destitute professional student is more amusing when you have someone with which to share it.

Working in a radiation oncology center he was able to recognize that his interests were in radiation protection and the safe use of ionizing radiation, and began to work towards a graduate degree in health physics at LSU. Andrew enrolled as a full-time student in January of 2014. Upon completion of his graduate studies, Andrew is going to work as a radiation health physicist for the Washington Department of Health in Olympia, Washington.